Notice:

This manuscript has been resubmitted to Geochemistry, Geophysics, Geosystems following peer review. Subsequent versions may differ in text and content, please check for the newest version before referencing this preprint.

Details:

Title: Lateral variations in lower crustal strength control the temporal evolution of mountain ranges: examples from south-east Tibet

Authors:

Camilla Penney (COMET, University of Cambridge)

Alex Copley (COMET, University of Cambridge)

Contact: cp451@cam.ac.uk

Submitted for publication in Geochemistry, Geophysics, Geosystems

Lateral variations in lower crustal strength control the temporal evolution of mountain ranges: examples from south-east Tibet

Camilla Penney[1]*, Alex Copley[1]

April 15, 2020

Key points:

- Lateral variations in lower crustal strength provide a first-order control on the shape and temporal evolution of mountain ranges.
- Strong lower crust in the Sichuan Basin can explain the development of topography in the Longmen Shan without a lower crustal channel.
- Lateral transport of samples should be considered in calculating and interpreting palaeoelevations from stable-isotope palaeoaltimetry.

*Corresponding author: cp451@cam.ac.uk, [1]COMET, Bullard Laboratories, Department of Earth Sciences, University of Cambridge, Cambridge, UK

Abstract

Controversy surrounds the rheology of the continental lithosphere, and how it controls the evolution and behaviour of mountain ranges. In this study, we investigate the effect of lateral contrasts in the strength of the lower crust, such as those between cratonic continental interiors and weaker rocks in the adjacent deforming regions, on the evolution of topography. We combine numerical modelling and recently published results from stable-isotope palaeoaltimetry in south-east Tibet. Stable-isotope palaeoaltimetry in this region provides constraints on vertical motions, which are required to distinguish between competing models for lithosphere rheology and deformation. We use numerical modelling to investigate the effect of lateral strength contrasts on the shape and temporal evolution of mountain ranges. In combination with palaeoaltimetry results, our modelling suggests that lateral strength contrasts provide a first-order control on the evolution of topography in south-east Tibet. We find that the evolution of topography in the presence of such strength contrasts leads to laterally-varying topographic gradients, and to key features of the GPS- and earthquake-derived strain-rate field, without the need for a low-viscosity, lower-crustal channel. We also find that palaeoaltimetric samples may have been transported laterally for hundreds of kilometres, an effect which should be accounted for in their interpretation. Our results are likely to be applicable to the evolution of mountain ranges in general, and provide an explanation for the spatial correlation between cratonic lowland regions and steep mountain range-fronts.

Plain Language Summary

The rocks which make up the Earth's continents move and change shape in response to tectonic forces. How rocks respond to these forces depends on their material properties, and can vary in space and time. These material properties, therefore, control the shape

of mountain ranges and how mountains grow. This study investigates why some mountain ranges have steep fronts, whilst others have gentle gradients. We look at how regions made up of strong rocks (such as the Sichuan Basin) affect the shape and growth of adjacent mountain ranges. We find that mountain ranges with steep fronts can form when weaker rocks move over stronger ones. Recent measurements of oxygen in ancient soils suggests that parts of the south-eastern margin of the Tibetan Plateau (between the Sichuan Basin and the Central Lowlands of Myanmar) have been high since about 50 million years ago, and that the area has risen more slowly than has previously been estimated. In south-east Tibet, the pattern of earthquakes, and how fast the mountains have grown, can be explained by these strong areas, without invoking complicated material properties in the mountain ranges. Such strong regions may be important in controlling the shape of mountain ranges globally.

1 Introduction

The strength of the lithosphere provides a first-order control on the distribution of strain within it. Strength, here, means resistance to deformation, which might be controlled by the stresses transmitted across faults in the brittle part of the lithosphere or the rheology associated with ductile creep in the lower crust and upper mantle. Lateral strength contrasts, such as those between anhydrous rocks in cratonic continental interiors, from which volatiles have been removed by previous partial melting, and more hydrous rocks in the adjacent deforming regions, are a feature of continental lithosphere globally. Such contrasts control the distribution of strain in the continents and, therefore, the evolution of mountain ranges (e.g. Vilotte et al., 1984; England and Houseman, 1985; Flesch et al., 2001; Jackson et al., 2008). Regions with strong crust, such as cratons, tend to accommodate little strain in comparison to their surroundings. In the India–Eurasia collision, for example, the accreted terranes which form the southern margin of Eurasia, rather than cratonic India, have accommodated most of the shortening. Here we investigate the effect of lateral contrasts in the strength of the lower crust on the temporal evolution of mountain belts.

A key outstanding question about the effect of lateral strength contrasts is how regions with strong lower crust, and the flow of less viscous material over and around them, affect the evolution of mountain ranges over tens of millions of years. Previous studies of continental deformation demonstrate that models which are able to reproduce instantaneous strain rates do not necessarily lead to the formation of the observed topography over time (e.g. Houseman and England, 1986; England and Houseman, 1986), so incorporating temporal evolution is an important extension to models considering the geologically-instantaneous effects of such contrasts (e.g. Copley, 2008; Bischoff and Flesch, 2019). Our interest is in understanding the physical controls on mountain building, and the constraints which recently-published stable-isotope palaeoaltimetry observations can provide on lithosphere rheology. Vertical motions, to which palaeoaltimetry observations are sensitive, have the potential to distinguish between rheological models which lead to the same horizontal surface velocities (Copley, 2008; Flesch et al., 2018). Understanding the implications of these observations, and the associated caveats is, therefore, critical to constraining lithosphere rheology. Numerical models with a small number of parameters allow us to test whether lower-crustal strength contrasts, consistent with observations, can reproduce variations in topographic gradients, or whether other driving mechanisms are required. In this study, we combine new palaeoaltimetry observations from south-east Tibet, with a simple 3D model of crustal deformation, to explore the effects of lateral strength contrasts in controlling continental deformation.

The south-eastern margin of the Tibetan plateau (south-east Tibet, Figure 1) is a good place to study the effect of lateral strength contrasts. Low elevations, relief and strain rates (both seismic – Figure 1 – and geodetic – Zheng et al., 2017; Maurin et al., 2010) in the

Sichuan Basin and the Central Lowlands of Myanmar suggest that these regions experience relatively little deformation. These regions are, therefore, likely to be strong in comparison to the high region between them, and the mountain belts which surround them, which have undergone significant recent and cumulative deformation. The Sichuan Basin is covered by $\sim$10 km of sediments (Hubbard and Shaw, 2009), underlain by Paleoproterozoic crust (Burchfiel et al., 1995) with high seismic velocities in the upper mantle (e.g. Lebedev and Nolet, 2003; Li and Van Der Hilst, 2010). Post-seismic motion after the 2008 Wenchuan earthquake suggests a strength contrast across the Longmen Shan (Huang et al., 2014), as do differences in elastic thickness between the Longmen Shan and the Sichuan Basin derived from gravity anomalies (Fielding and McKenzie, 2012).

Although the Central Lowlands of Myanmar have been less extensively studied than the Longmen Shan, the lack of topography, and the presence of undeformed Miocene sediments suggest low rates of post-Miocene deformation (Wang et al., 2014). Initial GPS measurements by Maurin et al. (2010) suggest that central Myanmar, west of the Sagaing fault, deforms in a coherent manner. Earthquakes in the Central Lowlands of Myanmar, shown in Figure 1b, are associated either with strike-slip motion on the Sagaing fault, on the eastern margin of the lowlands (which accommodates a component of the oblique India–Eurasia convergence; Maurin et al., 2010) or with active subduction beneath the Indo-Burman ranges (e.g. Stork et al., 2008; Steckler et al., 2016, yellow focal mechanisms in Figure 1b have depths >50 km). The seismic strain rate within the Central Lowlands is, therefore, low, at least in the instrumental period.

In contrast, the high regions of south-east Tibet deform rapidly, with kinematics described in detail by Copley (2008), who also summarised the work of previous authors. Since that study, numerous thrust-faulting earthquakes have occurred along the Longmen Shan, including the 2008 Wenchuan and 2013 Lushan earthquakes and their aftershocks (Figure 1). These earthquakes, and subsequent analysis of shortening on structures imaged in seismic profiles (Hubbard and Shaw, 2009), demonstrate that active shortening of the brittle upper crust is occurring across the Longmen Shan.

Much of the morphology of south-east Tibet is dominated by deeply-incised river valleys, often following the traces of strike-slip faults (Wang and Burchfiel, 1997). Collectively these strike-slip faults accommodate south-eastwards motion of high topography relative to both the Sichuan Basin and the Central Lowlands of Myanmar (e.g. Shen et al., 2005), with the faults on opposite sides of the high region accommodating opposite senses of shear (Figure 1a). The Xianshuihe and Sagaing faults (Figure 1a) have left- and right-lateral geodetic slip rates of $\sim$7–9 mm yr^{-1} and $\sim$18 mm yr^{-1} respectively (Zheng et al., 2017; Maurin et al., 2010). The region of distributed left-lateral faulting east of the Sagaing fault (Figure 1a) accommodates right-lateral shear on north-south striking planes through rotations about vertical axes (Copley, 2008).

A suite of models (e.g. Royden et al., 1997; Clark and Royden, 2000; Clark et al., 2005a) have focussed on the possibility of a low viscosity, lower-crustal channel producing the steep topography of the Longmen Shan, and the gentle topographic gradients to the south of the basin. By extending these channel flow models to include rigid regions, Cook and Royden (2008) argued for the importance of both a strong Sichuan Basin and flow in a mid/lower crustal channel, in the formation of steep topography across the Longmen Shan. Chen et al. (2013a) and Chen et al. (2013b) used 2D thermo-mechanical models with extrapolated laboratory flow laws to demonstrate that the craton was an important control on deformation in the region. We build up on this work by using a simple 3D model to isolate the effects of this rigid, cratonic region, and comparing the results to observational constraints from palaeoaltimetry.

Vertical velocities can distinguish between competing models of depth-dependent rheology which would lead to the same horizontal velocities (Copley, 2008; Flesch et al., 2018; Bischoff and Flesch, 2019). Copley (2008) demonstrated that rapid flow at depth associated with a weak mid-to-lower crust would lead to faster instantaneous vertical motions than coherent upper- and lower- crustal deformation. The specific rates were based on instantaneous calculations, so would not necessarily apply to the geologically-recorded uplift rates, but exemplify the possibility of using vertical motions to distinguish between different models of depth-dependent rheology.

Previous quantitative studies of topographic evolution in south-east Tibet have focussed on thermochronology (e.g. Kirby et al., 2002; Clark et al., 2004; Wang et al., 2012, 2016). Thermochronometric ages give information about exhumation, which is controlled by the interplay between tectonics and erosion. Such ages have been interpreted to imply that rapid uplift occurred $\sim$13–5 Ma, based on the identification of geomorphic surfaces presumed to have formed at low elevation (Clark et al., 2005a, 2006). However, it has been suggested that such low-relief, erosional surfaces can also form at high elevations (e.g. Liu-Zeng et al., 2008; Yang et al., 2015) and that increased exhumation may have been related to changes in the base level of rivers draining the region (e.g. Richardson et al., 2008). The interpretation of the existing thermochronometric data in terms of elevation history is therefore unclear. In this study we make use of new estimates of palaeoelevation from stable-isotope geochemistry, which provide an opportunity to quantitatively constrain the elevation history of south-east Tibet and, therefore, to distinguish between competing models of lithosphere rheology and mountain-range evolution.

We first summarise recently published results from stable-isotope palaeoaltimetry (Section 2) to constrain the uplift and elevation history of south-east Tibet. We then use fluid-dynamical modelling of the mountain range (described in Section 3) to investigate the effects of lateral strength contrasts on the evolution of topography through time, and compare our results to south-east Tibet (Section 4).

Although the results presented here are in the context of South East Tibet, the presence of lateral strength contrasts is a common feature of mountain ranges globally (e.g. Lamb, 2000; Jackson et al., 2008; Nissen et al., 2011). In particular, many mountain ranges, both active and older, have edges adjacent to cratons (McKenzie and Priestley, 2008). – regions of (often thick) continental lithosphere, usually composed of Proterozoic or Archean crust, which have remained relatively undeformed through multiple deformation cycles (Holmes, 1965). In section 5, therefore, we discuss that applicability of our results to the temporal evolution of mountain ranges in general.

2 Palaeoaltimetry

Stable-isotope palaeoaltimetry uses systematic variations in the isotopic composition of precipitation with elevation to derive the palaeoelevation of sample sites (e.g. Rowley et al., 2001). These techniques have been developed in order to place quantitative constraints on the elevation history of orogenies, such as Tibet, but they have not yet been extensively used as a constraint in dynamic models. South-east Tibet is a good region to carry out palaeoaltimetry studies. Moisture paths from the ocean to high topography in the region are simple, as the Rayleigh fractionation relationship between the oxygen-isotope composition of precipitation and elevation in present-day elevation transects shows (Hren et al., 2009).

Figure 2 shows results from six recent palaeoaltimetry studies in south-east Tibet, which use soil-deposited (Hoke et al., 2014; Xu et al., 2016; Tang et al., 2017; Gourbet et al., 2017) or lacustrine (Li et al., 2015; Xu et al., 2016; Gourbet et al., 2017; Wu et al., 2018) carbonates to derive the oxygen-isotope composition of palaeo-precipitation and, hence, palaeoelevations. In south-east Tibet, particularly in the Jianchuan Basin (Figure 1a), the age of sampled formations is a significant source of uncertainty (Hoke, 2018). Gourbet et al. (2017) revised the age of formations previously mapped as Miocene, and mid-Eocene, to the late Eocene, based on more precise dating (Figure 2b). As well as the direct uncertainty as to when a sample was deposited, hotter global temperatures in the Eocene (Savin, 1977; Miller et al., 1987; Zachos et al., 2001) alter the relationship between isotopic composition and elevation, resulting in different paleoelevation estimates (filled and unfilled symbols in Figure 2b show paleoelevation estimates calculated using modern and Eocene relationships respectively). However, the differences in palaeoelevation resulting from these hotter temperatures are generally much less than the kilometre scale of interest for dynamic modelling, even for upper-bound estimates of Eocene temperature (region 4, Figure 2b Hoke et al., 2014; Li et al., 2015; Tang et al., 2017; Wu et al., 2018).

$\delta^{18}O$ at sea level is also time-dependent. Licht et al. (2014) found very negative values of $\delta^{18}O$ in an Eocene gastropod and rhinoceroid from Myanmar, taken as sea level references for the time. Preliminary results from isotopic analysis of soil-deposited carbonates in the same area show similarly low $\delta^{18}O$ (Licht et al., 2019). A more negative starting value leads to lower palaeoelevation estimates, since Rayleigh fractionation predicts increasingly negative $\delta^{18}O$ with elevation. These improved estimates of starting composition, as well as the dating discussed above, have led to recalculations of palaeoelevation in south-east Tibet (Gourbet et al., 2017; Wu et al., 2018, shown as dark-outlined symbols in Figure 2b, the original estimates are shown with pale outlines), and we use these in our uplift rate calculations in preference to the original studies.

Uplift rates can be derived from stable-isotope palaeoaltimetry if samples can be taken from rocks of multiple ages at the same location. These rates, therefore, only reflect points in space and time which are preserved in the carbonate record. Where such rates can be inferred they are shown in Figure 2b. All of these inferred uplift rates are <0.3mm yr^{-1}.

In all the regions shown in Figure 2, except regions 5 and 6, which are the furthest to the south-east, paleoelevations similar present-day elevations are found in the oldest sampled formations. To the north-west (region 1), Tang et al. (2017) suggest that topography may have been high since before the Eocene. Although Xu et al. (2016)'s measurements have significant uncertainty in the moisture source, they suggest a lower bound for the elevation of the Longmen Shan of $\sim$3000 m, compared to present-day elevations of 2800-3700 m, in the late Miocene. To the south-east, region 5 may have experienced some uplift since the late Miocene, at rates <0.3 mm yr^{-1}, and region 6 was likely at its present elevation by the late Miocene.

These stable-isotope palaeoaltimetry results suggest that at least some areas of present-day south-east Tibet have been high since the late Eocene, and are likely to have reached present-day elevations prior to the onset of rapid exhumation inferred by Clark et al. (2005b) from the incision of river gorges (gray region in Figure 2b). Uplift rates across south-east Tibet are likely to have been much lower (<0.3 mm yr^{-1}) than would be predicted if all the uplift in the region had occurred since the late Miocene. Recently published thermochronology is also consistent with this palaeoaltimetric data, suggesting that topography across the Longmenshan had begun to develop by the Oligocene (Wang et al., 2012), and that uplift may have been ongoing since the Paleocene (Liu-Zeng et al., 2018).

3 Dynamical modelling

In tandem with the published palaeoaltimetry estimates summarised in section 2, we use numerical modelling to investigate the effect of lateral contrasts in lower crustal strength on the temporal evolution of mountain ranges. We first summarise the work of previous authors (section 3.1) and then describe the setup for the model used here (section 3.2) and our boundary conditions (section 3.3), before describing the model results in section 4. We emphasise that our model is intended to investigate the first-order effects of lateral strength contrasts on the multi-million-year development of long-wavelength topography in general, rather than to simulate the detailed evolution of south-east Tibet.

3.1 Previous Models

In regions of distributed deformation, the continental lithosphere can be modelled as a continuum (commonly a viscous fluid), with motion driven by horizontal pressure gradients – resulting from gravity acting on elevation contrasts – and by the relative motion of the bounding plates (e.g. England and McKenzie, 1982, 1983; Houseman and England, 1986; Royden et al., 1997; Lamb, 2000; Flesch et al., 2001; Reynolds et al., 2015; Flesch et al., 2018). Many authors use the thin-viscous-sheet model, which assumes negligible depth variations in horizontal velocities (England and McKenzie, 1982, 1983). This model implicitly assumes that the top and base of the lithosphere experience shear tractions which are small in comparison to other components of the deviatoric stress tensor (here referred to as a stress-free boundary condition, after McKenzie et al., 2000). In the model, this corresponds to flow over a less viscous fluid (the asthenosphere). Such models can only produce steep-fronted topography if the lithosphere has an effective power-law rheology with a high stress exponent (typically greater than 3, i.e. shear-thinning, e.g. Houseman and England, 1986; Lechmann et al., 2011). The typical gradients in these models are still much less steep than those in steep-fronted mountain ranges such as the Himalayas and the Longmen Shan (England and Houseman, 1986). Geologically, stress exponents greater than 1 are associated with rocks deforming by dislocation creep (e.g. Stocker and Ashby, 1973).

Steep topographic gradients often occur adjacent to lateral contrasts in lithosphere strength. Such regions are commonly associated with large gradients in crustal thickness, and, if less viscous material flows over a higher viscosity region, this is equivalent to flow over a rigid base (defined as zero-horizontal velocity, or no-slip, after McKenzie et al., 2000). In such regions the thin-viscous sheet approximation breaks down, because flow over a rigid base is accommodated by vertical gradients of horizontal velocity in the flowing layer. Medvedev and Podladchikov (1999a) presented an extension to the thin-viscous sheet model to allow for rapid spatial variations in material properties, which was applied to 2D geodynamic scenarios by Medvedev and Podladchikov (1999b). An alternative approach is to use full thermo-mechanical models in either 2D (e.g. Beaumont et al., 2001) or 3D (e.g. Lechmann et al., 2011; Pusok and Kaus, 2015). Here we discuss a simplified approach, which allows us to incorporate flow over both stress-free and rigid boundaries into a single 3D model with a small number of adjustable parameters.

Previous studies incorporating vertical gradients of horizontal velocity have focused on reproducing geologically-instantaneous deformation in south-east Tibet (e.g. Copley, 2008; Lechmann et al., 2014; Bischoff and Flesch, 2019). These studies have demonstrated that key features of the instantaneous earthquake- and GPS-derived velocity field can be explained by lateral viscosity contrasts between cratonic blocks and the surrounding mountain ranges. Studies which have investigate the effects of these cratonic blocks on the temporal evolution of topography in south-east Tibet have used complex models at the scale of entire collision zones (e.g. Pusok and Kaus, 2015), or imposed external forcing or velocities to drive the flow (e.g. Cook and Royden, 2008). Here, we use a simple model of 3D crustal deformation, described below, to isolate the effects of lateral strength contrasts on the evolution of topography through time. Our interest is in understanding the physical controls on topographic evolution, in particular the development of contrasting topographic gradients. Consideration of the time-evolution of the topography is important because it allows us to investigate the constraints which can be provided by newly-available palaeoaltimetry data.

3.2 Model Setup

We model the lithosphere as a viscous fluid. The geometry and boundary conditions we use are based on the long-wavelength topography of south-east Tibet (Figure 3). Using a geometry similar to south-east Tibet allows us to make use of the palaeoaltimetric results described in Section 2 in assessing the uplift rates associated with the model.

GPS velocities relative to Eurasia in south-east Tibet are sub-parallel to topographic gradients (Figure 3). Movement of material along topographic gradients suggests that the deformation in south-east Tibet is influenced by gravitational potential energy contrasts. The models we investigate here, therefore, include gravitational potential energy as a driving force; deformation in these models is driven by gravity acting on crustal thickness contrasts, without applied compressive forces or imposed boundary velocities. This category of models has been described by Lechmann et al. (2014) as "density driven". Analogous models have been applied since the 1980s to the gravitational spreading of crustal thrust sheets (e.g. Ramberg, 1981; Merle and Guillier, 1989). Here we consider deformation on the lithosphere scale, rather than the lengthscale of individual thrust sheets. These studies also considered analogues between glaciological and geological gravity-driven deformation, including the possibility of both stress-free and no-slip basal boundary conditions (Ramberg, 1981). We extend this analogy here by using methods from ice-sheet modelling to solve the governing equations.

We solve the Stokes' equations using the method proposed by Pattyn (2003), which includes vertical gradients of horizontal velocities (Appendix A). This method allows us to model flow over a stress-free base and also a rigid base, representing regions of strong lower crust, as suggested by Medvedev and Podladchikov (1999a), unlike the original thin-viscous-sheet model (England and McKenzie, 1982, 1983). Our method neglects horizontal derivatives of vertical velocities, which are expected to become important immediately adjacent to the change in basal boundary condition (Schmalholz et al., 2014). Pattyn (2003) demonstrated that the effect of these gradients being large is confined to a region over similar lateral extent to the thickness of the deforming layer (1–2 grid cells in our model), and that this does not affect the overall behaviour of the model.

The method we use here has previously been used to calculate instantaneous strain rates in south-east Tibet (Copley, 2008). Reynolds et al. (2015) extended this approach to model the temporal evolution of the Sulaiman Ranges by re-writing the incompressibility condition as a diffusion equation for topography (Pattyn, 2003). We use an improved method (described in detail in Appendix A) to solve this diffusion equation, calculating diffusivities on a staggered grid, and using the generalised minimum residual method (Saad and Schultz, 1986) to solve the resulting sparse matrix equations. We use a regular horizontal grid of 15 km$\times$15 km, and 20 grid points in the vertical, which are re-scaled at each time step

(Appendix A; Pattyn, 2003). The assumptions and set-up of this model are discussed below.

We model the deforming crust as an isoviscous, Newtonian fluid. Using a simple rheology allows us to test the extent to which topographic evolution in south-east Tibet is controlled by the presence of lateral lower crustal strength contrasts, and whether additional rheological complexity is required to explain the geophysical and geological observations. The simple rheology we use contrasts with the approach of previous authors studying the effect of a strong craton on the evolution of topography in south-east Tibet. For example, Chen et al. (2013a) used a 2D model with multiple rock types and an assumed geotherm. Cook and Royden (2008) included a weak lower crustal channel and drove deformation within their model through an imposed velocity at its base. By using a simpler rheology, we are able to isolate the effects of lower crustal strength contrasts on the evolution of topography. We discuss the possible effects of a more complicated rheology in Section 5. The velocity of the fluid is linearly dependent on the choice of viscosity, so although we use a viscosity of 10^{22} Pas here (as suggested for south-east Tibet by Copley and McKenzie, 2007), the models can be considered to apply to different viscosities by scaling the time and velocities. For example, the topography after 50 Myr of model evolution with a viscosity of 10^{22} Pas would be the same as that after 5 Myr for a viscosity of 10^{21} Pas. The velocities would be 10 times greater in the 10^{21} Pas case.

Figure 4 shows a schematic of our model setup. High viscosity regions, analogous to the lower crust of the Sichuan Basin and the Central Lowlands of Myanmar, are simulated by setting horizontal velocities to zero in part of the model with a specified thickness ("basal thickness", grey areas in Figure 4). Flow can occur over and around these rigid regions ("basins", Basin E and Basin W in Figure 4). The basal thickness is equivalent to the thickness of strong lower crust. The Sichuan Basin is connected to the South China craton (e.g.

Li and Van Der Hilst, 2010), which provides a resistive force, so the basins in our model are not advected with the flow. By setting velocities to zero in these basin regions, we are assuming that the Sichuan Basin and Central Lowlands of Myanmar have behaved rigidly over the 50 Myr of deformation which we model. This approach is suggested by inferences of strong lower crust and upper mantle in the Sichuan Basin and Central Lowlands of Myanmar (Section 1; Li and Van Der Hilst, 2010; Huang et al., 2014). We use crustal thicknesses in the Longmen Shan and Sichuan Basin of 65 and 36–40 km respectively (e.g. Liu et al., 2014), with 4.5 km of elevation contrast, and a constant crustal density, $\rho_c = 2700$ kg m^{-3}, to determine the lower crustal viscosity required for our assumption of rigidity to hold. The buoyancy force associated with this crustal thickness contrast can be calculated by integrating the pressure difference between the two columns of crust (e.g. Artyushkov, 1973; Molnar and Tapponnier, 1978; Dalmayrac and Molnar, 1981), giving a maximum buoyancy force of 7×10^{12} N m^{-1}. This buoyancy force results in a maximum normal stress of 200 MPa acting on the Sichuan Basin. If this topographic contrast has existed since 50 Mya (the effective start time of our model) then for the Sichuan Basin, which is ∼300 km wide, to have deformed by less than one grid cell in our model (15 km), requires a strain rate in the lower crust, $\dot{\epsilon} \leq 3.2 \times 10^{-17}$ s^{-1}. In this scenario the viscosity of the crust in the Sichuan Basin would need to be greater than 6×10^{24} Pas to remain undeformed by buoyancy forces associated with crustal thickness contrasts. The viscosity required would be lower if the topographic contrast were supported for a shorter time. We can test whether this viscosity is reasonable using laboratory-derived flow laws. We use the dry flow laws for typical lower crustal minerals from Bystricky and Mackwell (2001) and Rybacki et al. (2006), and calculate the temperature corresponding to a viscosity of 6×10^{24} Pas at the Moho (36–40 km Liu et al., 2014), assuming lithostatic pressure and a grain size of 1 mm. For both flow laws, the viscosity will be $\geq 6 \times 10^{24}$ Pas if the temperature is less than ∼800–900°C. Moho temperatures in undeforming Precambrian crust are typically ∼600°C (McKenzie et al., 2005), meaning that the viscosity required for the Sichuan Basin to behave rigidly on the timescales of our model is consistent with laboratory-derived flows laws. Rather than adding an additional parameter to our model we therefore model the basin lower crust as rigid. As discussed in section 1, the geological structure of the Central Myanmar Basin is less well constrained than that of the Sichuan Basin, but it also acts in a rigid manner, so for simplicity we make the same assumption there.

Outside the basins, the base of the current is stress-free (England and McKenzie, 1982, 1983; Copley and McKenzie, 2007), implying that the asthenosphere imposes negligible shear stress on the base of the lithosphere. Since we only model the deformation of the crust, a further assumption is that the crust and lithospheric mantle deform coherently in the region with the stress-free base. In this case, vertical planes in the lithosphere will deform by pure shear. Since the horizontal velocities will not vary with depth, the effect of imposing a stress-free boundary condition at the base of the crust is the same as imposing this condition at the base of the lithosphere (because we assume isostatic compensation at the Moho, see below). Copley (2008) demonstrated the possibility of coherent lower crust and lithospheric mantle deformation in south-east Tibet with rheologies extrapolated from laboratory flow laws. Although such extrapolations lead to vertical gradients in viscosity, in many cases these gradients, and the length-scales over which they occur, are insufficient to result in appreciable contrasts in horizontal velocities.

The top surface of the current is stress-free throughout the model domain, representing the lack of significant tractions imposed by the atmosphere. We track particles on this surface, which move with the horizontal velocity at their location at each time step. These particles are analogous to the samples used in palaeoaltimetric studies.

We impose isostatic compensation at the base of the crust relative to a column of mantle

(Flesch et al., 2001), with densities of 2700 kg m^{-3} and 3300 kg m^{-3} respectively. Assuming isostatic compensation neglects flexural support of the topography. By using a viscous model, we are implicitly considering long-wavelength deformation (motivated by the long-wavelength shape of the topography in Figure 3). Free-air gravity anomalies from south-east Tibet suggest that flexure plays a role in supporting the topography on relatively short-wavelengths ($\sim$50 km into the Longmen Shan), which means that isostatic compensation is an appropriate assumption thoroughout most of the model domain. At the edge of the basin region, where flexural support may be important, flexure would be expected to give a shape for the basal boundary intermediate between full isostatic compensation, which we use here, and a base which cannot move vertically in response to loading, a case which is often considered in the fluid dynamics literature (e.g. Huppert, 1982). The implications of assuming isostatic compensation are discussed in Section 4.

In some models we investigate the interaction between erosion and propagation of the current by incorporating an erosive term;

$$\frac{\partial s}{\partial t} = -\kappa \left| \nabla s \right|, \tag{1}$$

where κ is a constant. Gradient-dependent erosion is suggested by higher erosion rates and greater cumulative erosion in the Longmen Shan than in the interior of the Sichuan Basin and Tibetan Plateau (Richardson et al., 2008). This erosive term has the same derivation as the classic Culling model (Culling, 1960), but assumes that eroded material is removed from the model domain. This assumption is consistent with Hubbard et al.'s (2010) proposal that sediment is transported away from the Sichuan basin by the Yangtze River.

3.3 Lateral Boundary Conditions

The mathematical details of the boundary conditions used in our model are given in Appendix A. Here we summarise these boundary conditions and explain their physical motivation.

Initially ($t = 0$), the domain is filled with a 40 km-thick layer of fluid (H_0, Figure 4), chosen to represent generic, undeformed continental crust. There may have been pre-existing topography in south-east Tibet before the onset of Cenozoic deformation (Burchfiel et al., 1995; Hubbard et al., 2010). However, the shape of this topography is poorly constrained, so we assume an initially uniform layer for simplicity.

At one edge of the model domain ($y = 0$) fluid flows into the region, analogous to the lateral growth of a mountain range, in this case from central Tibet into south-east Tibet. The height of the influx ($y = 0$) boundary is kept constant over time. The normal stress on this boundary is set by the buoyancy force associated with a reservoir of high material (i.e. the central Tibetan Plateau), which can supply fluid to the current at the same rate at which fluid moves away from the boundary (Figure 4; Reynolds et al., 2015). The reference elevation along this boundary, S_0, is 4.5 km above the surface of the 40 km thick layer in the remainder of the model domain, similar to the mean elevation of the Tibetan Plateau above the Sichuan Basin (Figure 1). The starting topography within the model domain adjacent to this influx boundary has a constant slope in the y direction (Figure 4); its gradient does not affect the model results after the first few timesteps. Using a fixed-height boundary condition is analogous to assuming that the central Tibetan plateau acts as a reservoir of lithosphere, and has been at its present elevation throughout the development of high topography in south-east Tibet. This simple assumption allows us to isolate the effects of lateral variations in lower-crustal strength in south-east Tibet, and is consistent with palaeoaltimetric data, which suggest that the central plateau has been high since at least the Eocene (e.g. Rowley and Currie, 2006). We set the velocity parallel to this boundary to zero ($u = 0$ on $y = 0$), motivated by the small velocity component parallel to the NW boundary of Figure 3.

At the right-hand end of the domain as shown in Figure 4 ($y = y_{max}$), and beyond the basins ($y > y_b$), the normal stress on the boundaries is set by the buoyancy force associated with 40 km-thick crust outside the model domain (e.g. Artyushkov, 1973; Molnar and Tapponnier, 1978; Dalmayrac and Molnar, 1981; Turcotte and Schubert, 2014). This condition is equivalent to the model domain being surrounded by 40 km-thick crust and experiencing the associated buoyancy force at the domain boundaries. Using the buoyancy force to set the normal stress perpendicular to the boundary, rather than anti-parallel to the maximum topographic gradient, implicitly assumes that the maximum topographic gradient is perpendicular to the boundary. We find that this assumption has little effect on the modelling results, and makes the calculations much less computationally expensive because we do not need to iterate over the velocity calculation at each timestep. However, making this assumption does mean that we require a second condition for the boundary-parallel velocity. We set the derivatives of boundary-parallel velocities perpendicular to these boundaries to zero (i.e. $\frac{\partial u}{\partial y} = 0$ on $y = y_{max}$, and $\frac{\partial v}{\partial x} = 0$ on $x = 0$ and $x = x_{max}$). This second condition is equivalent to assuming that the crust outside the model domain does not exert significant shear stresses on the domain boundary. These boundary conditions are consistent with the lack of significant zones of strike-slip deformation outside the region of south-east Tibet which corresponds to our model domain (Figure 3).

Along $x = 0$ and $x = x_{max}$ we use a reflection boundary condition up to the end of the basins ($y < y_b$). This is equivalent to assuming that mountains also exist to either side of the model domain, and are behaving in the same manner in these regions; analogous to high topography existing to the north of the Sichuan Basin and the Central Lowlands of Myanmar.

4 Results & Comparison to South East Tibet

We initially use symmetric models (i.e. where the two basins with strong lower crust have the same size and are the same distance from the influx boundary) to investigate the effects of changing basal thickness and inter-basin width (defined in Figure 4) on the evolution of topography. Figure 5 shows the results of a model with symmetric basins of radius 450 km (grey semi-circles, Figure 5c, equivalent to an inter-basin width of 600 km), and basal thickness 15 km. Times referred to are since the start of the model and elevations are given relative to the surface of 40 km-thick, isostatically-compensated crust. As discussed in Section 3, the velocity and, therefore, the rate of topographic evolution, scale linearly with the viscosity. The topography after 50 Myr of model evolution with a viscosity of 10^{22} Pas (as shown in Figure 5a) would correspond to that after 5 Myr for a viscosity of 10^{21} Pas.

Regions with a stress-free base develop gentle topographic gradients. Deformation in these regions is effectively by pure shear of vertical planes; gentle topographic gradients result from the quasi-depth-independent horizontal velocities. Gentle topographic gradients are also a feature of thin-viscous-sheet models (England and McKenzie, 1982, 1983, even where these models use high stress-exponents; Section 3.1), which have the same, stress-free, basal boundary condition. The topographic gradients in the stress-free regions are very similar in magnitude to the south-eastwards topographic gradients in the high region between the Sichuan Basin and the Central Lowlands of Myanmar (compare Figures 6h and 6f – the topographic profile location is shown in Figure 2a).

In contrast, steep topographic gradients develop in the basin regions, suggesting that steep topography can form as a result of mountain ranges overriding rigid lower crust. The different topographic gradients which develop in regions with and without a rigid base (compare Figures 6a, c and e to Figures 6b, d and f), are consistent with previous work showing that flow over a rigid base results in steeper gradients than flow over a stress-free base (e.g. McKenzie et al., 2000). The topography also propagates more slowly in the basin regions than in the region between them (compare Figure 6 c and d). These effects arise because where flow occurs over a rigid base, the velocity depends on the square of the flow depth (Huppert, 1982). Increasing the basal thickness, analogous to having a thicker rigid lower crust or a thinner overlying layer of deformable rock, therefore, reduces the distance which the current propagates into the basin in a given time, and also results in steeper topographic profiles where the flow overrides the basin. This effect is demonstrated by Figure 6, which shows profiles through models with the same basin locations as in Figure 5, but with varying basal thicknesses. The locations of these profiles are shown in Figure 5b. The lateral extent of the region which has a rigid base is shown by grey bars on the profiles. Figures 6 a & b, c & d and e & f have basal thicknesses of 0 km (only the base is rigid), 15 km and 30 km respectively. A proportionally thicker rigid region (e.g. Figure 6e) means that the current is flowing into a thinner fluid layer, so tends to develop a sharper nose, as shown by McKenzie et al. (2000). The topographic gradients across the Longmen Shan (Figures 6g) are very similar to those in our model for a basal thickness of 30 km (corresponding to 10 km initial thickness of deformable rock in the basin regions). This basal thickness is consistent with ~10 km of sediment overlying Paleoproterozoic basement in the Sichuan Basin (Hubbard and Shaw, 2009).

Erosion also leads to steeper topographic gradients, and hinders current propagation in the basins. The dashed lines in Figure 6c and d show the results of eroding the topography with $\kappa = 4$ mm yr^{-1} in equation (1). The erosive term we use is proportional to gradient (Section 3), meaning that the steep slopes in the basins are affected more than gentle slopes in the inter-basin region (compare dashed lines in Figures 6c and d). With κ =4 mm yr^{-1} the topography is quasi-stationary on the basin margins between 15 and 50 Myr (dashed blue and red lines in Figure 6c), demonstrating that erosion can stop the propagation of topography in these regions (as suggested by Koons, 1989, for the South Island of New Zealand), but not in the region of fast flow between the basins. The similar position of the present-day Longmen Shan and the Paleogene deformation front adjacent to the Sichuan Basin (derived from stratigraphic thicknesses of foreland basin sediments; Richardson et al., 2008) could, therefore, result from erosion acting on topography which would otherwise be propagating over the basin. Such an effect is possible because of the slow propagation of topography over rigid lower crust.

The distance between basins also controls the velocity of the current. Figure 7 shows the topographic and velocity profiles resulting from different inter-basin widths, with constant basal thickness (15 km). Greater inter-basin widths result in faster velocities perpendicular to the profile (v, Figures 7b, d, f). Flow in the inter-basin region is dominated by simple shear of horizontal planes – similar to that between two rigid walls (Copley and McKenzie, 2007), with maximum velocity proportional to width squared. The width of the rapidly deforming region between the Sichuan Basin and the Central Lowlands of Myanmar is $\sim$500 km. Observed GPS velocities relative to Eurasia in the centre of this region are $\sim$20 mm yr^{-1}. Inter-basin velocities in our model are similar to these GPS velocities for an inter-basin width of 600 km, which suggests that the viscosity we use for our modelling (10^{22} Pas) is reasonable.

As discussed in section 3.2, these models do not include flexural support of the topography. If we did include flexural support we would not expect to see qualitatively different topography, because the wavelengths associated with such support are small in comparison to the scale of our model. Viscous models of the crust, such as the one we use here, implicitly investigate long wavelength deformation, at scales longer than individual faults (Figure 3, England and McKenzie, 1982, 1983). Gravity anomalies demonstrate flexural effects in south-east Tibet acting on wavelengths less than ∼50 km (Fielding and McKenzie, 2012), and isostatic compensation throughout the region of high topography (Jordan and Watts, 2005; Fielding and McKenzie, 2012). Fielding and McKenzie (2012) found a lower bound on the elastic thickness of the Sichuan Basin of 10 km (although this value is poorly constrained since the basin is too small for the full flexural wavelength to be measured) and an elastic thickness of 7 km for the adjacent high topography. Flexure may provide local support to the topography where it overthrusts the Sichuan Basin (in our model, over the horizontally rigid basin). The topographic gradient in this region of our model, therefore, represents an end-member in which the rigid (zero horizontal velocity) base is free to move vertically. The other end-member, in which the base cannot move vertically in response to being loaded, also leads to steep fronts (Huppert, 1982), even when flow is into a layer which is much thicker the the topography (McKenzie et al., 2000). The rigid nature of the basal boundary (i.e. the no-slip condition on the base of the fluid) controls the shape of the topography, rather than whether or not this boundary is able to deform vertically (McKenzie et al., 2000). Ball et al. (2019) demonstrated that flexural effects are primarily important near the nose of a viscous current, but that such currents over a flexed base can still form steep topographic gradients as long as the base of the current has a no-slip boundary condition. The difference in basal boundaries conditions, and the depth of deformable rock, therefore, provide a first-order explanation for contrasting topographic gradients in south-east Tibet, even if our models do not capture the precise, short-wavelength details of the topography.

The elevation histories of particles we track at the surface of the current (Figure 5d) show that uplift rates from our model are ∼0.1–0.5 mm yr^{-1} in the centre of the inter-basin region (red star in Figure 5d), similar to the < 0.3 mm yr^{-1} uplift rates derived from palaeoaltimetry (Section 2, Figure 2). However, our modelling also demonstrates that the interpretation of palaeoelevation results is not straightforward. Figure 5 shows that material at the surface may be transported long distances (hundreds of kilometres over tens of millions of years for the viscosity used here). The advection of particles with the flow means that elevation histories may be complex, with particle elevations decreasing "south" (towards $y = y_{max}$) of the inter-basin region as the current spreads laterally (the same effect which leads to the extensional strain rates described below). Pedogenic carbonates which are found to have been high in the late Eocene–early Miocene (Hoke et al., 2014; Li et al., 2015; Gourbet et al., 2017) could have been deposited at similar latitudes to samples from the Longmen Shan, which were at their present elevation in the late Miocene (Xu et al., 2016).

By considering the principal axes of the horizontal the strain-rate tensor at the surface of our model (Figure 5b) as analogous to the strain rate in the brittle crust (Houseman and England, 1986), we can draw comparisons between our model and the geodetic- and seismic-strain rates in south-east Tibet. The largest strain-rates in both our model and in south-east Tibet are associated with shear at the basin margins. Strain rates equivalent to left-lateral shear adjacent to Basin E (Figure 4), and right-lateral shear adjacent to Basin W (Figure 4) are analogous to left-lateral slip on the Xianshuihe Fault and right-lateral slip on the Nuijiang and Sagaing Faults (and adjacent right-lateral faults) respectively.

Compressive strain rates associated with steep topography at the edges of the basins are small in comparison to these shear strain rates. In the context of south-east Tibet this suggests that the steep topography, and low shortening rates, across the Longmen Shan could result from flow of weaker material, with a coherently-deforming upper and lower crust, over the rigid lower crust of the Sichuan Basin (Copley and McKenzie, 2007; Copley, 2008; Fielding and McKenzie, 2012), without a low-viscosity, lower-crustal channel.

The principal axes of the horizontal strain-rate tensor at the surface of our models show two extension-dominated regions (red ellipses in Figure 5b), with similar locations and orientations to the normal faulting in south-east Tibet (red ellipses and focal mechanisms in Figure 1b). The extensional strain rates in these parts of our model are ∼2–5 times larger than the compressional strain rates, so these regions are equivalent to mixed strike-slip and normal faulting, with normal faulting dominating. Extension in the y direction 'north' of the basins (top white ellipse in Figure 5b) is comparable to the northern group of normal faults in Figure 1, which strike perpendicular to both topographic gradient (accommodating extension parallel to the topographic gradient) and GPS velocities relative to Eurasia (Figure 3). Our modelling suggests that this extension may result from a velocity increase where the topography is confined in the inter-basin region. The second region of extension occurs where fluid spreads out laterally to the 'south' of the basins; increasing the surface area of the current. This extension perpendicular to topographic gradients is shown by the bottom white ellipse in Figure 5b. The southern group of normal faults shown in Figure 1 also accommodate extension perpendicular to the topographic gradients.

Figure 8 shows the results of changing the shape of one of the basins to be more similar to that of the Central Lowlands of Myanmar. The region of shear which develops adjacent to this basin is broader than that adjacent to a semi-circular basin because the flow is approximately parallel to the change in basal boundary condition, resulting in greater horizontal tractions on vertical planes. This broader region of shear is similar to the area of distributed left-lateral faulting east of the Sagaing fault (Figure 1a), which accommodates right-lateral shear through vertical-axis rotations (Copley, 2008). The lateral extent of this shear in south-east Tibet may, therefore, be controlled by the geometry of the rigid lower crust in the Central Lowlands of Myanmar.

5 Discussion

Our model allows us to reproduce the main features of the present-day topography, strain-rate and velocity field in south-east Tibet, and uplift rates from palaeoaltimetry. These results demonstrate that lateral strength contrasts, in the form of regions of rigid lower crust, provide a first-order control on the temporal evolution of mountain ranges (Figure 9). Below we discuss our key findings and their application to mountain ranges in general.

In our model, which has mechanically-coupled upper and lower crust, surface uplift rates are <0.5 mm yr^{-1}. These gradual uplift rates are consistent with palaeoaltimetry results in south-east Tibet, suggesting that no low-viscosity, lower-crustal channel is required to explain to evolution of topography in this region. However, the results of particle tracking show that material at the surface where the crust flows over a stress-free base may be transported long distances (hundreds of kilometres over millions of years for the viscosity used here, consistent with fault offsets reported over shorter time periods, Wang and Burchfiel, 1997). Calculated palaeoelevations, therefore, estimate the palaeoelevation of the place where the sample was deposited, rather than the palaeoelevation of its present-day location. Accounting for this lateral transport is also important for converting the oxygen-isotope composition of carbonates to palaeoelevation, potentially requiring greater continentality corrections. Although strike-slip faults do not build mountains, they can move them horizontally for large distances.

Our modelling demonstrates that differences in basal boundary condition, analogous to the presence or absence of strong lower crust, can lead to the development of contrasting topographic gradients. In particular, steep gradients arise naturally from flow over a rigid (no-slip) base. The present-day compressional strain rates across these steep margins are low in comparison to the rates of shear where deformation is parallel to the basin margins, in both our model and in south-east Tibet (Shen et al., 2005; Zheng et al., 2017). This combination, of steep-fronted topography and low compressional strain rates, is a feature of other parts of the India-Eurasia collision. Steep topographic gradients adjacent to the Tarim basin (∼3 km over 50 km) and the low rate of shortening (0–3 mm yr^{-1}, e.g. Zheng et al., 2017) across the basin margin are similar to those in the Longmen Shan. Increasing Moho depths from north to south across the margin (Wittlinger et al., 2004), and the flexural signal seen in free-air gravity anomalies (e.g. McKenzie et al., 2019), suggests that the western edge of the Tarim Basin may underthrust the western Kunlun ranges, which would provide a rigid base to the flow of crustal material from northern Tibet, in a similar manner to the Sichuan Basin in south-east Tibet. The temporal evolution of topography adjacent to the Tarim Basin may, therefore, also be controlled by the lateral strength contrast between rigid lower crust in the Tarim Basin and lower viscosity crust in Tibet. The motion of southern Tibet over rigid India is likely to represent the same effect. However, the rates of motion in southern Tibet are more rapid than in northern Tibet, perhaps due to differences in the thicknesses, temperatures or compositions of the crust in India and the Tarim basin.

More generally, the control on topographic evolution provided by lateral strength contrasts, particularly the low rates of propagation of topography into regions with rigid lower crust (Figures 6, 9), suggests an explanation for the correlation of cratonic regions with steep edges of mountain belts (including the Atlas mountains, the Caucasus and older orogenies such as the Appalachians and Rockies in North America) noted by McKenzie and Priestley

(2008). Cratonic regions are likely to have relatively strong lower crust (e.g. Jackson et al., 2008), so our results suggest that the propagation of topography into these regions will be slow in comparison to adjacent regions where the lower crust has lower viscosity.

We also find that the thickness of strong lower crust, and of deformable material (such as sediments) above it, controls the extent of mountain range propagation and the morphology of the range front. Larger thicknesses of deformable rock (fluid layer above the rigid base in our models) lead to more rapid propagation of topography over regions with strong lower crust, and to shallower topographic gradients. This result is likely to apply to mountain ranges globally. The occurrence of thin-skinned deformation of sediments above the edges of the South American craton, in the foothills of the Eastern Cordillera of the Andes (Lamb, 2000), suggests that the deformation in this region is comparable to flow over a rigid base. The foothills in the southern Bolivian Andes extend further east than those in the north, and have lower topographic gradients. This broader foothill region correlates with higher sediment thicknesses in the bounding basin (McGroder et al., 2014), similar to the current in our model propagating further over a rigid base where the deformable layer is thicker (Figure 6c and e). Along-strike variations in sediment thickness can also explain variations in the morphology of the Indo-Burman Ranges (Ball et al., 2019), although there mountain building is driven by the subducting plate, which advects sediment laterally, as well as by contrasts in gravitational potential energy. Ball et al. (2019) highlighted that it is the thickness of deformable sediment, rather than the total sediment thickness, which is important in controlling morphology. Although beyond the scope of this study, we expect that along-strike variations in the viscosity of the deformable rock, as well as its thickness, could lead to similar changes in morphology. In the Zagros mountains, for example, along-strike variations in the width of high topography could potentially correlate with the presence or absence of weak salt layers (Nissen et al., 2011). Similarly, the prominent curvature of the

Sulaiman Ranges, and their projection beyond the general ∼north–south strike of the Pakistan range front, has been proposed to result from a weaker package of sediments beneath them (Reynolds et al., 2015).

For crust in this tectonic setting, it is not clear whether ductile deformation is dominated by diffusion creep, which is Newtonian with a stress exponent of 1, or dislocation creep, which has a power-law rheology with a stress exponent greater than 1, (e.g. Stocker and Ashby, 1973). In our modelling, we have, therefore, taken the simplest approach, which is to use a Newtonian rheology with a constant viscosity. Our models show that such a rheology can produce steep topographic gradients where flow occurs over a rigid base, such as strong lower crust. In contrast, in models where depth variations in horizontal velocity are neglected, steep topographic gradients require a power-law rheology with a high stress exponent, and, even then, these gradients are much shallower than those in the Longmen Shan (Section 3.1, Houseman and England, 1986; England and Houseman, 1986; Lechmann et al., 2011). If dislocation creep does control ductile deformation, the vertically-integrated strength of the lithosphere can be represented as a single power-law rheology (Sonder and England, 1986). An interesting question, therefore, is whether the steep topographic gradients in our model would still form if we had used a power-law, rather than a Newtonian, rheology. A higher stress-exponent would tend to localise deformation in regions of high strain rate, such as immediately above the rigid lower crust in the basin regions. The second invariant of the strain rate tensor in these regions of our model is $\sim 10^{-15}$ s^{-1}, consistent with geodetically- and geologically-estimated strain rates in tectonically active regions (Fagereng and Biggs, 2019). For a viscosity of 10^{22} Pas this strain rate corresponds to a stress of ~ 10 MPa, typical of earthquake stress drops (Kanamori and Anderson, 1975; Allmann and Shearer, 2009). If the crust were to deform with a power-law rheology with a stress-exponent of 3, and assuming a strain rate in the rest of the model domain of $\sim 10^{-16}$ s^{-1}, these strain rates would lead to a local drop in viscosity from 10^{22} Pas to $\sim 2 \times 10^{21}$ Pas, which might lubricate the base of the current. However, the flow over the rigid base would still be much slower than that with a stress-free base, and have a non-linear dependence on the thickness of the current, meaning that we would still expect contrasting topographic gradients to develop. Mathematical studies of gravity currents composed of power-law fluids suggest that, although there may be some increase in far-field surface slope associated with such effects, flow over a rigid base nonetheless tends to produce a steep front (Gratton et al., 1999). Our result, that steep topographic gradients can form with a Newtonian rheology, therefore, suggests that steep-fronted mountain ranges do not constrain whether flow in the ductile part of the lithosphere occurs by diffusion or dislocation creep, but does demonstrate that the presence of strong lower crust can explain first-order contrasts in topographic gradients.

6 Conclusion

We have investigated the role of lateral contrasts in lower crustal strength in controlling the shape and evolution of mountain ranges. In south-east Tibet, stable-isotope palaeoaltimetry suggests that parts of the topography may have been at, or near, their present-day elevations since the late Eocene and that uplift is likely to have occurred more slowly than had previously been inferred. In combination with a simple model, these results demonstrate that lateral strength contrasts are sufficient to explain first-order features of the deformation and topographic evolution in south-east Tibet, without invoking a low-viscosity, lower-crustal channel. Since our models of topographic evolution in the presence of lateral lower-crustal strength contrasts allow us to reproduce the main features of the present day topography, strain-rate and velocity field in south-east Tibet, we suggest that lateral strength contrasts provide a first-order control on the temporal evolution and shape of mountain ranges. Our modelling also suggests that lateral contrasts in lower crustal strength provide an explanation for the correlation between cratons and the steep gradients on the edges of some mountain ranges.

Acknowledgements

C.P. would like to thank Thomasina Ball and Jerome Neufeld for helpful discussions. This work forms part of the NERC- and ESRC-funded project 'Earthquakes without Frontiers' and was partially supported by the NERC large grant 'Looking inside the Continents from Space'. C.P. is funded by a Junior Research Fellowship from Queens' College, University of Cambridge and was funded by a NERC studentship for part of the research. Figures were prepared using the GMT package (Wessel et al., 2013). No data was created for this research. Palaeoaltimetry data can be found in Hoke et al. (2014); Li et al. (2015); Xu et al. (2016); Tang et al. (2017); Gourbet et al. (2017); Wu et al. (2018). Earthquake focal mechanisms can be found in Copley (2008) (and references therein), Zhang et al. (2010), Li et al. (2011), Han et al. (2014), Bai et al. (2017), Han et al. (2018), the CMT catalogue (Dziewonski et al., 1981; Ekström et al., 2012) and the ISC-EHB catalogue (Engdahl et al., 1998; International Seismological Centre, 2016). GPS data in Figure 3 are from Zheng et al. (2017).

A Time evolution of a viscous current

We solve the Stokes' flow equations, neglecting horizontal variations in vertical velocity, following the method proposed by Pattyn (2003) for glaciers. We briefly outline this method below in order to demonstrate how our model results are calculated and to highlight some possible simplifications.

In a Cartesian co-ordinate system, (x, y, z), the horizontal velocities (u, v) are related to gradients of the surface height, s, through:

$$4\frac{\partial\eta}{\partial x}\frac{\partial u}{\partial x}+\frac{\partial\eta}{\partial y}\frac{\partial u}{\partial y}+\frac{\partial\eta}{\partial z}\frac{\partial u}{\partial z}+\eta\left(4\frac{\partial^2}{\partial x^2}+\frac{\partial^2}{\partial y^2}+\frac{\partial^2}{\partial z^2}\right)u=\rho g\frac{\partial s}{\partial x}-2\frac{\partial\eta}{\partial x}\frac{\partial v}{\partial y}-\frac{\partial\eta}{\partial y}\frac{\partial v}{\partial x}-3\eta\frac{\partial^2 v}{\partial x\partial y} \quad (1)$$

and

$$4\frac{\partial\eta}{\partial y}\frac{\partial v}{\partial y}+\frac{\partial\eta}{\partial x}\frac{\partial v}{\partial x}+\frac{\partial\eta}{\partial z}\frac{\partial u}{\partial z}+\eta\left(\frac{\partial^2}{\partial x^2}+4\frac{\partial^2}{\partial y^2}+\frac{\partial^2}{\partial z^2}\right)v=\rho g\frac{\partial s}{\partial y}-\frac{\partial\eta}{\partial x}\frac{\partial u}{\partial y}-2\frac{\partial\eta}{\partial y}\frac{\partial u}{\partial x}-3\eta\frac{\partial^2 u}{\partial x\partial y} \quad (2)$$

(equations 18 and 19 of Pattyn, 2003) where η and ρ are the viscosity and density of the fluid respectively, and g is the gravitational acceleration. We follow Pattyn in scaling the vertical dimension at each timestep (cf. his equation 44). We then solve the resulting velocity equations at each timestep (subject to the boundary conditions discussed below and in section 3.3) using the generalised minimum residual method (Saad and Schultz, 1986, in sparskit2).

We include the full form of these equations here to illustrate the general, variable viscosity case. However, since we consider the constant viscosity case here, $\nabla\eta = \mathbf{0}$ and these equations can be simplified to

$$\eta \left(4\frac{\partial^2}{\partial x^2} + \frac{\partial^2}{\partial y^2} + \frac{\partial^2}{\partial z^2} \right) u = \rho g \frac{\partial s}{\partial x} - 3\eta \frac{\partial^2 v}{\partial x \partial y} \tag{3}$$

and

$$\eta \left(\frac{\partial^2}{\partial x^2} + 4\frac{\partial^2}{\partial y^2} + \frac{\partial^2}{\partial z^2} \right) v = \rho g \frac{\partial s}{\partial y} - 3\eta \frac{\partial^2 u}{\partial x \partial y}. \tag{4}$$

Taking partial derivatives of the incompressibility condition,

$$\frac{\partial u}{\partial x} + \frac{\partial v}{\partial y} + \frac{\partial w}{\partial z} = 0, \tag{5}$$

with respect to x and y, and using the conditions $\frac{\partial w}{\partial x}, \frac{\partial w}{\partial y} = 0$ (section 3.2) gives

$$\frac{\partial^2 u}{\partial x^2} + \frac{\partial^2 v}{\partial x \partial y} = 0, \tag{6}$$

and

$$\frac{\partial^2 v}{\partial y^2} + \frac{\partial^2 u}{\partial y \partial x} = 0. \tag{7}$$

Equations (3) and (4) then reduce to

$$\left(\frac{\partial^2}{\partial x^2} + \frac{\partial^2}{\partial y^2} + \frac{\partial^2}{\partial z^2} \right) u = \frac{\rho g}{\eta} \frac{\partial s}{\partial x} \tag{8}$$

and

$$\left(\frac{\partial^2}{\partial x^2} + \frac{\partial^2}{\partial y^2} + \frac{\partial^2}{\partial z^2} \right) v = \frac{\rho g}{\eta} \frac{\partial s}{\partial y}. \tag{9}$$

Pattyn (2003) proposed rewriting the incompressibility condition as a diffusion equation for topography. This approach allows the diffusivities to be calculated on a staggered grid, preventing leapfrog instabilities in the second-order finite differences. From integrating the incompressibility condition (5) over the layer thickness, H (Figure 4):

$$\frac{\partial H}{\partial t} = -\nabla_h \cdot (H\bar{u}, H\bar{v}), \tag{10}$$

where bars denote vertical averaging, and

$$\nabla_h = \left(\frac{\partial}{\partial x}, \frac{\partial}{\partial y}\right). \tag{11}$$

Equation (10) can be written as a diffusion equation for the topography, which Pattyn (2003) expressed as:

$$\frac{\partial H}{\partial t} = \nabla_h \cdot \left(D_x \frac{\partial H}{\partial x}, D_y \frac{\partial H}{\partial y}\right) + \nabla_h \cdot \left(D_x \frac{\partial b}{\partial x}, D_y \frac{\partial b}{\partial y}\right), \tag{12}$$

(his equation 55, where we make the derivatives explicit here for clarity), and:

$$D_x = \left|\bar{u}H\left(\frac{\partial s}{\partial x}\right)^{-1}\right|,$$
$$D_y = \left|\bar{v}H\left(\frac{\partial s}{\partial y}\right)^{-1}\right|,$$

(the modulus signs were implied but not included in Pattyn, 2003). In the glacier case for which this method was developed there is no prescribed relationship between the surface height, s, and bed depth, b (although $H = s + b$). However, for an isostatically-compensated fluid, such as the crust of south-east Tibet (e.g. Jordan and Watts, 2005), $b = -fs$ and $H = (1+f)\,s$, where$f = \frac{\rho_c}{\rho_m - \rho_c}$. For standard crust and mantle densities of 2700 kg m^{-3} and

3300 kg m^{-3} respectively, $f = 4.5$, which is what we assume here. Substituting these relationships into (12) gives

$$\frac{\partial H}{\partial t} = \left(\frac{1}{f+1}\right)\left(\partial_x\left(D_x \partial_x H\right) + \partial_y\left(D_y \partial_y H\right)\right). \tag{13}$$

We note that the diffusivities could alternatively have been defined as

$$D'_x = \left|\bar{u}H\left(\frac{\partial H}{\partial x}\right)^{-1}\right|,$$
$$D'_y = \left|\bar{v}H\left(\frac{\partial H}{\partial y}\right)^{-1}\right|,$$

in which case

$$\frac{\partial H}{\partial t} = \left(\partial_x\left(D'_x \partial_x H\right) + \partial_y\left(D'_y \partial_y H\right)\right). \tag{14}$$

$D_n = 0, n \in \{x, y\}$ becomes infinite if $\frac{\partial s}{\partial n} = 0$, but physically the topography in such regions should not propagate (i.e. $\frac{\partial H}{\partial t} = 0$, since in regions of flat topography there are no pressure contrasts to drive the flow). In such cases, therefore, we set $D_n = 0$.

We write equation (13) as a sparse matrix equation using a Crank-Nicolson scheme for the finite differences, with diffusivities calculated on a staggered grid, the approach suggested by Pattyn (2003). Solving both x and y terms in the same linear system, rather than separating the components means that the matrix does not have a simple form (the separated case is tridiagonal, which was the form used by Reynolds et al., 2015). We therefore solve this sparse system using the generalised minimum residual method (Saad and Schultz, 1986).

Boundary Conditions

Pressure Boundary conditions

Noting that the NW and SE margins of the region we study are isostatically compensated (e.g. Jordan and Watts, 2005), we impose the deviatoric stress resulting from integrated pressure differences between fluid in the domain and an assumed reservoir outside the domain on $y \in \{0, y_{max}\}$ and $x \in \{0, x_{max}\}$ for $y > y_b$ (where y_b denotes the far end of the basin, Figure 4). The buoyancy force exerted by a column of thickness H_0 on a column with thickness $H = H_0 - \Delta H$ is

$$\begin{aligned}\int_{-b}^{s} \Delta p \, dz &= -\frac{g\rho_c}{2}\left(1 - \frac{\rho_c}{\rho_m}\right)\left(H_0^2 - (H_0 - \Delta H)^2\right) \\ &= -\frac{g\rho_c}{2\,(1+f)} \Delta H \,(2H_0 - \Delta H)\,, \qquad (15)\end{aligned}$$

(e.g. Artyushkov, 1973; Molnar and Tapponnier, 1978; Dalmayrac and Molnar, 1981; Turcotte and Schubert, 2014, Figure A.1), where p is the lithostatic pressure, giving an associated deviatoric stress

$$\Delta\sigma_{yy} = -\frac{g\rho_c}{2H\,(1+f)} \Delta H \,(2H_0 - \Delta H) = 2\eta \frac{\partial v}{\partial y}, \qquad (16)$$

on boundaries in y, and

$$\Delta\sigma_{xx} = -\frac{g\rho_c}{2H\,(1+f)} \Delta H \,(2H_0 - \Delta H) = 2\eta \frac{\partial u}{\partial x}, \qquad (17)$$

on boundaries in x. We define tensional stresses as positive. Note that ΔH could be negative if the reference thickness is less than the thickness of the adjacent material, as is initially the case on the outflux boundaries. For the outflux boundaries, $H_0 = 40$ km. For the influx ($y = 0$) boundary $H_0 = 65$ km (corresponding to 4.5 km surface relief above 40 km thick crust). Ideally, we would impose the stress condition on the outflux boundary anti-parallel to the direction of flow, to represent a uniform reservoir of unthickened crust i.e. the direction normal to the outflux domain boundaries has no particular physical or geological significance. We impose the pressure condition on the normal stress for simplicity. As a result, these boundary conditions determine only the boundary-perpendicular velocities, and we require a further condition on the boundary-parallel velocities. For the influx boundary, we set $u = 0$. For the outflux boundaries we set $\frac{\partial v}{\partial x} = 0$ on $x \in \{0, x_{max}\}$ and $\frac{\partial u}{\partial y} = 0$ on $y = y_{max}$. Since the far-field part of the domain is not substantially thickened by the end of our modelling, velocities adjacent to these far-field boundaries are small and we expect that imposing the stresses anti-parallel to the flow would not substantially alter our results.

Reflection Boundary conditions

On $x \in \{0, x_{max}\}$ we use reflection boundary conditions $u = 0$, $\frac{\partial v}{\partial x} = 0$ for $y < y_b$. We impose the condition on u directly. As shown above, for constant viscosity, v is given by equation (9), which can be further simplified by considering

$$u\big|_{x=0} = 0 \Rightarrow \left.\frac{\partial u}{\partial y}\right|_{x=0} = 0 \Rightarrow \frac{\partial^2 u}{\partial x \partial y} = 0,$$

which, from (7), implies that $\frac{\partial^2 v}{\partial y^2} = 0$. Equation (9) therefore reduces to

$$\left(\frac{\partial^2}{\partial x^2} + \frac{\partial^2}{\partial z^2}\right) v = \frac{\rho g}{\eta}\frac{\partial s}{\partial y}, \tag{18}$$

which we solve in its co-ordinate transformed form.

References

Allmann, B. P. and Shearer, P. M. (2009). Global variations of stress drop for moderate to large earthquakes. *J. Geophys. Res. Solid Earth*, 114(1):1–22.

Artyushkov, E. V. (1973). Stresses in the lithosphere caused by crustal thickness inhomogeneities. *J. Geophys. Res.*, 78(32):7675–7708.

Bai, L., Li, G., Khan, N. G., Zhao, J., and Ding, L. (2017). Focal depths and mechanisms of shallow earthquakes in the Himalayan-Tibetan region. *Gondwana Res.*, 41:390–399.

Ball, T. V., Penney, C. E., Neufeld, J. A., and Copley, A. C. (2019). Controls on the geometry and evolution of thin-skinned fold-thrust belts, and applications to the Makran accretionary prism and Indo–Burman Ranges. *Geophys. J. Int.*, 218(1):247–267.

Beaumont, C., Jamieson, R. A., Nguyen, M. H., and Lee, B. (2001). Himalayan tectonics explained by extrusion of a low-viscosity crustal channel coupled to focused surface denudation. *Nature*, 414(6865):738–742.

Bischoff, S. and Flesch, L. (2019). Impact of Lithospheric Strength Distribution on India-Eurasia Deformation From 3-D Geodynamic Models. *J. Geophys. Res. Solid Earth*, 124(1):1084–1105.

Burchfiel, B. C., Zhiliang, C., Yupinc, L., and Royden, L. H. (1995). Tectonics of the Longmen Shan and Adjacent Regions, Central China. *Int. Geol. Rev.*, 37(8):661–735.

Bystricky, M. and Mackwell, S. (2001). Creep of dry clinopyroxene aggregates with deformation in the dislocation creep. *J. Geophys. Res.*, 106:13443–13454.

Chen, L., Gerya, T., Zhang, Z., Zhu, G., Duretz, T., and Jacoby, W. R. (2013a). Numerical modeling of eastern Tibetan-type margin: Influences of surface processes, lithospheric structure and crustal rheology. *Gondwana Res.*, 24(3-4):1091–1107.

Chen, L., Gerya, T. V., Zhang, Z. J., Aitken, A., Li, Z. H., and Liang, X. F. (2013b). Formation mechanism of steep convergent intracontinental margins: Insights from numerical modeling. *Geophys. Res. Lett.*, 40(10):2000–2005.

Clark, M. K., Bush, J. W. M., and Royden, L. H. (2005a). Dynamic topography produced by lower crustal flow against rheological strength heterogeneities bordering the Tibetan Plateau. *Geophys. J. Int.*, 162:575–590.

Clark, M. K., House, M. A., Royden, L. H., Whipple, K. X., Burchfiel, B. C., Zhang, X., and Tang, W. (2005b). Late Cenozoic uplift of southeastern Tibet. *Geology*, 33(6):525–528.

Clark, M. K. and Royden, L. H. (2000). Topographic ooze: Building the eastern margin of Tibet by lower crustal flow. *Geology*, 28(8):703.

Clark, M. K., Royden, L. H., Whipple, K. X., Burchfiel, B. C., Zhang, X., and Tang, W. (2006). Use of a regional, relict landscape to measure vertical deformation of the eastern Tibetan Plateau. *J. Geophys. Res. Earth Surf.*, 111:F03002.

Clark, M. K., Schoenbohm, L. M., Royden, L. H., Whipple, K. X., Burchfiel, B. C., Zhang, X., Tang, W., Wang, E., and Chen, L. (2004). Surface uplift, tectonics, and erosion of eastern Tibet from large-scale drainage patterns. *Tectonics*, 23:TC1006.

Cook, K. L. and Royden, L. H. (2008). The role of crustal strength variations in shaping orogenic plateaus, with application to Tibet. *J. Geophys. Res. Solid Earth*, 113(8):1–18.

Copley, A. (2008). Kinematics and dynamics of the southeastern margin of the Tibetan Plateau. *Geophys. J. Int.*, 174:1081–1100.

Copley, A. and McKenzie, D. (2007). Models of crustal flow in the India-Asia collision zone. *Geophys. J. Int.*, 169:683–698.

Culling, W. E. H. (1960). Analytical Theory of Erosion. *J. Geol.*, 68(3):336–344.

Dalmayrac, B. and Molnar, P. (1981). Parallel thrust and normal faulting in Peru and constraints on the state of stress. *Earth Planet. Sci. Lett.*, 55:473–481.

Dziewonski, A. M., Chou, T., and Woodhouse, J. H. (1981). Determination of earthquake source parameters from waveform data for studies of global and regional seismicity. *J. Geophys. Res.*, 86(B4):2825–2852.

Ekström, G., Nettles, M., and Dziewoński, A. M. (2012). The global CMT project 2004-2010: Centroid-moment tensors for 13,017 earthquakes. *Phys. Earth Planet. Inter.*, 200-201:1–9.

Engdahl, E. R., van der Hilst, R., and Buland, R. (1998). Global teleseismic earthquake relocation with improved travel times and procedures for depth determination. *Bull. Seismol. Soc. Am.*, 88(3):722–743.

England, P. and Houseman, G. (1985). Role of lithospheric strength heterogeneities in the tectonics of Tibet and neighbouring regions. *Nature*, 315:297–301.

England, P. and Houseman, G. (1986). Finite strain calculations of continental deformation: 2. Comparison with the India-Asia Collision Zone. *J. Geophys. Res. Solid Earth*, 91(B3):3664–3676.

England, P. and McKenzie, D. (1982). A thin viscous sheet model for continental deformation. *Geophys. J. Int.*, 70:295–321.

England, P. and McKenzie, D. (1983). Correction to: a thin viscous sheet model for continental deformation. *Geophys. J. R. Astr. Soc.*, 73:523–532.

Fagereng, Å. and Biggs, J. (2019). New perspectives on 'geological strain rates' calculated from both naturally deformed and actively deforming rocks. *J. Struct. Geol.*, 125(January 2018):100–110.

Fielding, E. J. and McKenzie, D. (2012). Lithospheric flexure in the Sichuan Basin and Longmen Shan at the eastern edge of Tibet. *Geophys. Res. Lett.*, 39:L09311.

Flesch, L., Bendick, R., and Bischoff, S. (2018). Limitations on Inferring 3D Architecture and Dynamics From Surface Velocities in the India-Eurasia Collision Zone. *Geophys. Res. Lett.*, 45:1379–1386.

Flesch, L. M., Haines, J. A., and Holt, W. E. (2001). Dynamics of the India-Eurasia Shortening. *J. Geophys. Res.*, 106(B8):16,435–16,460.

Gourbet, L., Hervé, P., Paquette, J.-L., Sorrel, P., Maheo, G., Wang, G., Yadong, X., Cao, K., Antoine, P.-O., Eymard, I., Liu, W., Lu, H., Replumaz, A., Chevalier, M.-L., Kexin, Z., Jing, W., and Shen, T. (2017). Reappraisal of the Jianchuan Cenozoic basin stratigraphy and its implications on the SE Tibetan plateau evolution. *Tectonophysics*, 700-701:162–179.

Gratton, J., Minotti, F., and Mahajan, S. M. (1999). Theory of creeping gravity currents of a non-Newtonian liquid. *Phys. Rev. E - Stat. Physics, Plasmas, Fluids, Relat. Interdiscip. Top.*, 60(6):6960–6967.

Han, L., Cheng, J., An, Y., Fang, L., Jiang, C., Chen, B., Wu, Z., Liu, J., Xu, X., Liu, R., Yao, Z., Wang, C., and Wang, Y. (2018). Preliminary Report on the 8 August 2017 Ms 7.0 Jiuzhaigou, Sichuan, China, Earthquake. *Seismol. Res. Lett.*, 89(2A):557–569.

Han, L., Zeng, X., Jiang, C., Ni, S., Zhang, H., and Long, F. (2014). Focal Mechanisms of the 2013 Mw 6.6 Lushan, China Earthquake and High-Resolution Aftershock Relocations. *Seismol. Res. Lett.*, 85(1):8–14.

Hoke, G. D. (2018). Geochronology transforms our view of how Tibet's southeast margin evolved. *Geology*, 46(1):95–96.

Hoke, G. D., Liu-Zeng, J., Hren, M. T., Wissink, G. K., and Garzione, C. N. (2014). Stable isotopes reveal high southeast Tibetan Plateau margin since the Paleogene. *Earth Planet. Sci. Lett.*, 394:270–278.

Holmes, A. (1965). *The Principles of Physical Geology.* Nelson, Edinburgh.

Houseman, G. and England, P. (1986). Finite strain calculations of continental deformation. 1. Method and general results for convergence zones. *J. Geophys. Res.*, 91(B3):3651–3663.

Hren, M. T., Bookhagen, B., Blisniuk, P. M., Booth, A. L., and Chamberlain, C. P. (2009). δ18O and δD of streamwaters across the Himalaya and Tibetan Plateau: Implications for moisture sources and paleoelevation reconstructions. *Earth Planet. Sci. Lett.*, 288:20–32.

Huang, M. H., Bürgmann, R., and Freed, A. M. (2014). Probing the lithospheric rheology across the eastern margin of the Tibetan Plateau. *Earth Planet. Sci. Lett.*, 396:88–96.

Hubbard, J. and Shaw, J. H. (2009). Uplift of the Longmen Shan and Tibetan plateau, and the 2008 Wenchuan (M = 7.9) earthquake. *Nature*, 458:194–197.

Hubbard, J., Shaw, J. H., and Klinger, Y. (2010). Structural setting of the 2008 Mw7.9 Wenchuan, China, earthquake. *Bull. Seismol. Soc. Am.*, 100(5B):2713–2735.

Huppert, H. E. (1982). The propagation of two-dimensional and axisymmetric viscous gravity currents over a rigid horizontal surface. *J. Fluid Mech.*, 121:43–58.

International Seismological Centre (2016). EHB Bulletin.

Jackson, J., McKenzie, D., Priestley, K., and Emmerson, B. (2008). New views on the structure and rheology of the lithosphere. *J. Geol. Soc. London.*, 165:453–465.

Jordan, T. A. and Watts, A. B. (2005). Gravity anomalies, flexure and the elastic thickness structure of the India-Eurasia collisional system. *Earth Planet. Sci. Lett.*, 236(3-4):732–750.

Kanamori, H. and Anderson, D. (1975). Theoretical basis of some empirical relations in seismology. *B. Seism. Soc. Am.*, 65(5):1073–1095.

Kirby, E., Reiners, P. W., Krol, M. A., Whipple, K. X., Hodges, K. V., Farley, K. A., Tang, W., and Chen, Z. (2002). Late Cenozoic evolution of the eastern margin of the Tibetan Plateau: Inferences from 40 Ar/ 39 Ar and (U-Th)/He thermochronology. *Tectonics*, 21(1):1001–1019.

Koons, P. O. (1989). The topographic evolution of collisional mountain belts: a numerical look at the Southern Alps, New Zealand. *Am. J. Sci.*, 289(9):1041–1069.

Lamb, S. (2000). Active deformation in the Bolivian Andes, South America. *J. Geophys. Res. Solid Earth*, 105(B11):25627–25653.

Lebedev, S. and Nolet, G. (2003). Upper mantle beneath Southeast Asia from S velocity tomography . *J. Geophys. Res. Solid Earth*, 108(B1).

Lechmann, S. M., May, D. A., Kaus, B. J., and Schmalholz, S. M. (2011). Comparing thin-sheet models with 3-D multilayer models for continental collision. *Geophys. J. Int.*, 187(1):10–33.

Lechmann, S. M., Schmalholz, S. M., Hetényi, G., May, D. A., and Kaus, B. J. P. (2014). Quantifying the impact of mechanical layering and underthrusting on the dynamics of the modern India-Asia collisional system with 3-D numerical models. *J. Geophys. Res. Solid Earth*, 119(1):616–644.

Li, C. and Van Der Hilst, R. D. (2010). Structure of the upper mantle and transition zone beneath Southeast Asia from traveltime tomography. *J. Geophys. Res. Solid Earth*, 115(7):1–19.

Li, S., Currie, B. S., Rowley, D. B., and Ingalls, M. (2015). Cenozoic paleoaltimetry of the SE margin of the Tibetan Plateau: Constraints on the tectonic evolution of the region. *Earth Planet. Sci. Lett.*, 432:415–424.

Li, Z., Elliott, J. R., Feng, W., Jackson, J. A., Parsons, B. E., and Walters, R. J. (2011). The 2010 Mw 6.8 Yushu (Qinghai, China) earthquake: Constraints provided by InSAR and body wave seismology. *J. Geophys. Res. Solid Earth*, 116:B10302.

Licht, A., Botsyun, S., Littell, V., Sepulchre, P., Donnadieu, Y., Risi, C., Rugenstein, J. K. C., Page, M., Huntington, K. W., and Nivet, G. D. (2019). Is Tibetan Plateau uplift more recent than we thought? In *AGU Fall Meet. Abstr.*

Licht, A., van Cappelle, M., Abels, H. A., Ladant, J.-B., Trabucho-Alexandre, J., France-Lanord, C., Donnadieu, Y., Vandenberghe, J., Rigaudier, T., Lécuyer, C., Terry Jr, D., Adriaens, R., Boura, A., Guo, Z., Soe, A. N., Quade, J., Dupont-Nivet, G., and Jaeger, J.-J. (2014). Asian monsoons in a late Eocene greenhouse world. *Nature*, 513(7519):501–506.

Liu, Q. Y., van der Hilst, R. D., Li, Y., Yao, H. J., Chen, J. H., Guo, B., Qi, S. H., Wang, J., Huang, H., and Li, S. C. (2014). Eastward expansion of the Tibetan Plateau by crustal flow and strain partitioning across faults. *Nat. Geosci.*, 7:361–365.

Liu-Zeng, J., Tapponnier, P., Gaudemer, Y., and Ding, L. (2008). Quantifying landscape differences across the Tibetan plateau: Implications for topographic relief evolution. *J. Geophys. Res. Earth Surf.*, 113:F04018.

Liu-Zeng, J., Zhang, J., McPhillips, D., Reiners, P., Wang, W., Pik, R., Zeng, L., Hoke, G., Xie, K., Xiao, P., Zheng, D., and Ge, Y. (2018). Multiple episodes of fast exhumation since Cretaceous in southeast Tibet, revealed by low-temperature thermochronology. *Earth Planet. Sci. Lett.*, 490:62–76.

Maurin, T., Masson, F., Rangin, C., Min, U. T., and Collard, P. (2010). First global positioning system results in northern Myanmar: Constant and localized slip rate along the Sagaing fault. *Geology*, 38(7):591–594.

McGroder, M. F., Lease, R. O., and Pearson, D. M. (2014). Along-strike variation in structural styles and hydrocarbon occurrences, Subandean fold-and-thrust belt and inner foreland, Colombia to Argentina. In *Geol. Soc. Am. Mem.*, volume 212, pages 79–113.

McKenzie, D., Jackson, J., and Priestley, K. (2005). Thermal structure of oceanic and continental lithosphere. *Earth Planet. Sci. Lett.*, 233:337–349.

McKenzie, D., McKenzie, J., and Fairhead, D. (2019). The Mechanical Structure of Tibet. *Geophys. J. Int.*, pages 950–969.

McKenzie, D., Nimmo, F., Jackson, J. A., Gans, P. B., and Miller, E. L. (2000). Characteristics and consequences of flow in the lower crust. *J. Geophys. Res. Solid Earth*, 105(B5):11029–11046.

McKenzie, D. and Priestley, K. (2008). The influence of lithospheric thickness variations on continental evolution. *Lithos*, 102:1–11.

Medvedev, S. E. and Podladchikov, Y. Y. (1999a). New extended thin-sheet approximation for geodynamic applications–I. Model formation. *Geophys. J. Int.*, 136(3):586–608.

Medvedev, S. E. and Podladchikov, Y. Y. (1999b). New extended thin-sheet approximation for geodynamic applications-II. Two-dimensional examples. *Geophys. J. Int.*, 136(3):586–608.

Merle, O. and Guillier, B. (1989). The building of the Central Swiss Alps: an experimental approach. *Tectonophysics*, 165(1-4):41–56.

Miller, K. G., Fairbanks, R. G., and Mountain, G. S. (1987). Tertiary Oxygen Isotope Synthesis, Sea Level History, and Continental Margin Erosion. *Paleoceanography*, 2(1):1–19.

Molnar, P. and Tapponnier, P. (1978). Active Tectonics of Tibet. *J. Geophys. Res.*, 83(B11).

Nissen, E., Tatar, M., Jackson, J., and Allen, M. (2011). New views on earthquake faulting in the Zagros fold-and-thrust belt of Iran. *Geophys. J. Int.*, 186:928–944.

Pattyn, F. (2003). A new three-dimensional higher-order thermomechanical ice sheet model: Basic sensitivity, ice stream development, and ice flow across subglacial lakes. *J. Geophys. Res.*, 108(B8):1–15.

Pusok, A. E. and Kaus, B. J. P. (2015). Development of topography in 3-D continental-collision models. *Geochemistry, Geophys. Geosystems*, 16(5):1378–1400.

Ramberg, H. (1981). The role of gravity in orogenic belts. *Geol. Soc. Spec. Publ.*, 9:125–140.

Reynolds, K., Copley, A., and Hussain, E. (2015). Evolution and dynamics of a fold-thrust belt: The Sulaiman Range of Pakistan. *Geophys. J. Int.*, 201:683–710.

Richardson, N. J., Densmore, A. L., Seward, D., Fowler, A., Wipf, M., Ellis, M. A., Yong, L., and Zhang, Y. (2008). Extraordinary denudation in the Sichuan Basin: Insights from low-temperature thermochronology adjacent to the eastern margin of the Tibetan Plateau. *J. Geophys. Res. Solid Earth*, 113:B04409.

Rowley, D. B. and Currie, B. S. (2006). Palaeo-altimetry of the late Eocene to Miocene Lunpola basin, central Tibet. *Nature*, 439:677–681.

Rowley, D. B., Pierrehumbert, R. T., and Currie, B. S. (2001). A new approach to stable isotope-based paleoaltimetry: Implications for paleoaltimetry and paleohypsometry of the High Himalaya since the late Miocene. *Earth Planet. Sci. Lett.*, 188:253–268.

Royden, L. H., Burchfiel, B. C., King, R. W., Wang, E., Chen, Z., Shen, F., and Liu, Y. (1997). Surface Deformation and Lower Crustal Flow in Eastern Tibet. *Science (80-.).*, 276(5313):788–790.

Rybacki, E., Gottschalk, M., Wirth, R., and Dresen, G. (2006). Influence of water fugacity and activation volume on the flow properties of fine-grained anorthite aggregates. *J. Geophys. Res. Solid Earth*, 111(3).

Saad, Y. and Schultz, M. H. (1986). GMRES: A Generalized Minimal Residual Algorithm for Solving Nonsymmetric Linear Systems. *SIAM J. Sci. Stat. Comput.*, 7(3):856–869.

Savin, S. M. (1977). The History of the Earth's Surface Temperature During the Past 100 Million Years. *Annu. Rev. Earth Planet. Sci.*, 5(1):319–355.

Schmalholz, S. M., Medvedev, S., Lechmann, S. M., and Podladchikov, Y. (2014). Relationship between tectonic overpressure, deviatoric stress, driving force, isostasy and gravitational potential energy. *Geophys. J. Int.*, 197(2):680–696.

Shen, Z. K., Lü, J., Wang, M., and Bürgmann, R. (2005). Contemporary crustal deformation around the southeast borderland of the Tibetan Plateau. *J. Geophys. Res. Solid Earth*, 110:B11409.

Sonder, L. J. and England, P. (1986). Vertical averages of rheology of the continental lithosphere: relation to thin sheet parameters. *Earth Planet. Sci. Lett.*, 77:81–90.

Steckler, M. S., Mondal, D. R., Akhter, S. H., Seeber, L., Feng, L., Gale, J., Hill, E. M., and Howe, M. (2016). Locked and loading megathrust linked to active subduction beneath the Indo-Burman Ranges. *Nat. Geosci.*, 9:615–618.

Stocker, R. L. and Ashby, M. F. (1973). On the rheology of the upper mantle. *Rev. Geophys.*, 11(2):391–426.

Stork, A. L., Selby, N. D., Heyburn, R., and Searle, M. P. (2008). Accurate relative earthquake hypocenters reveal structure of the Burma subduction zone. *Bull. Seismol. Soc. Am.*, 98(6):2815–2827.

Tang, M., Liu-Zeng, J., Hoke, G. D., Xu, Q., Wang, W., Li, Z., Zhang, J., and Wang, W. (2017). Paleoelevation reconstruction of the Paleocene-Eocene Gonjo basin, SE-central Tibet. *Tectonophysics*, 712-713:170–181.

Turcotte, D. and Schubert, G. (2014). Body Forces and Surface Forces. In *Geodynamics*, chapter 2, pages 93–98. Cambridge University Press, 3rd edition.

Vilotte, J. P., Daignieres, M., Madariaga, R., and Zienkiewicz, O. C. (1984). The role of a heterogeneous inclusion during continental collision. *Phys. Earth Planet. Inter.*, 36:236–259.

Wang, E. and Burchfiel, B. C. (1997). Interpretation of Cenozoic Tectonics in the Right-Lateral Accommodation Zone Between the Ailao Shan Shear Zone and the Eastern Himalayan Syntaxis. *Int. Geol. Rev.*, 39(3):191–219.

Wang, E., Kirby, E., Furlong, K. P., Van Soest, M., Xu, G., Shi, X., Kamp, P. J. J., and Hodges, K. V. (2012). Two-phase growth of high topography in eastern Tibet during the Cenozoic. *Nat. Geosci.*, 5:640–645.

Wang, Y., Sieh, K., Tun, S. T., Lai, K.-Y., and Myint, T. (2014). Active tectonics and earthquake potential of the Myanmar region. *J. Geophys. Res. Solid Earth*, 119:3767–3822.

Wang, Y., Zhang, B., Schoenbohm, L. M., Zhang, J., Zhou, R., Hou, J., and Ai, S. (2016). Late Cenozoic tectonic evolution of the Ailao Shan-Red River fault (SE Tibet): Implications for kinematic change during plateau growth. *Tectonics*, 35:1969–1988.

Wessel, P., Smith, W. H. F., Scharroo, R., Luis, J., and Wobbe, F. (2013). Generic Mapping Tools: Improved version released. *EOS Trans. AGU*, 94(45):409–410.

Wittlinger, G., Vergne, J., Tapponnier, P., Farra, V., Poupinet, G., Jiang, M., Su, H., Herquel, G., and Paul, A. (2004). Teleseismic imaging of subducting lithosphere and Moho offsets beneath western Tibet. *Earth Planet. Sci. Lett.*, 221(1-4):117–130.

Wu, J., Zhang, K., Xu, Y., Wang, G., Garzione, C. N., Eiler, J., Leloup, P. H., Sorrel, P., and Mahéo, G. (2018). Paleoelevations in the Jianchuan Basin of the southeastern Tibetan Plateau based on stable isotope and pollen grain analyses. *Palaeogeogr. Palaeoclimatol. Palaeoecol.*, 510(March):93–108.

Xu, Q., Liu, X., and Ding, L. (2016). Miocene high-elevation landscape of the eastern Tibetan Plateau. *Geochemistry, Geophys. Geosystems*, 17(10):4254–4267.

Yang, R., Willett, S. D., and Goren, L. (2015). In situ low-relief landscape formation as a result of river network disruption. *Nature*, 520:526–529.

Zachos, J., Pagani, H., Sloan, L., Thomas, E., and Billups, K. (2001). Trends, rhythms, and aberrations in global climate 65 Ma to present. *Science (80-.).*, 292(5517):686–693.

Zhang, P.-Z., Wen, X.-Z., Shen, Z.-K., and Chen, J.-H. (2010). Oblique, High-Angle, Listric-Reverse Faulting and Associated Development of Strain: The Wenchuan Earthquake of May 12, 2008, Sichuan, China. *Annu. Rev. Earth Planet. Sci.*, 38(1):353–382.

Zheng, G., Wang, H., Wright, T. J., Lou, Y., Zhang, R., Zhang, W., Shi, C., Huang, J., and Wei, N. (2017). Crustal Deformation in the India-Eurasia Collision Zone From 25 Years of GPS Measurements. *J. Geophys. Res. Solid Earth*, 122(11):9290–9312.

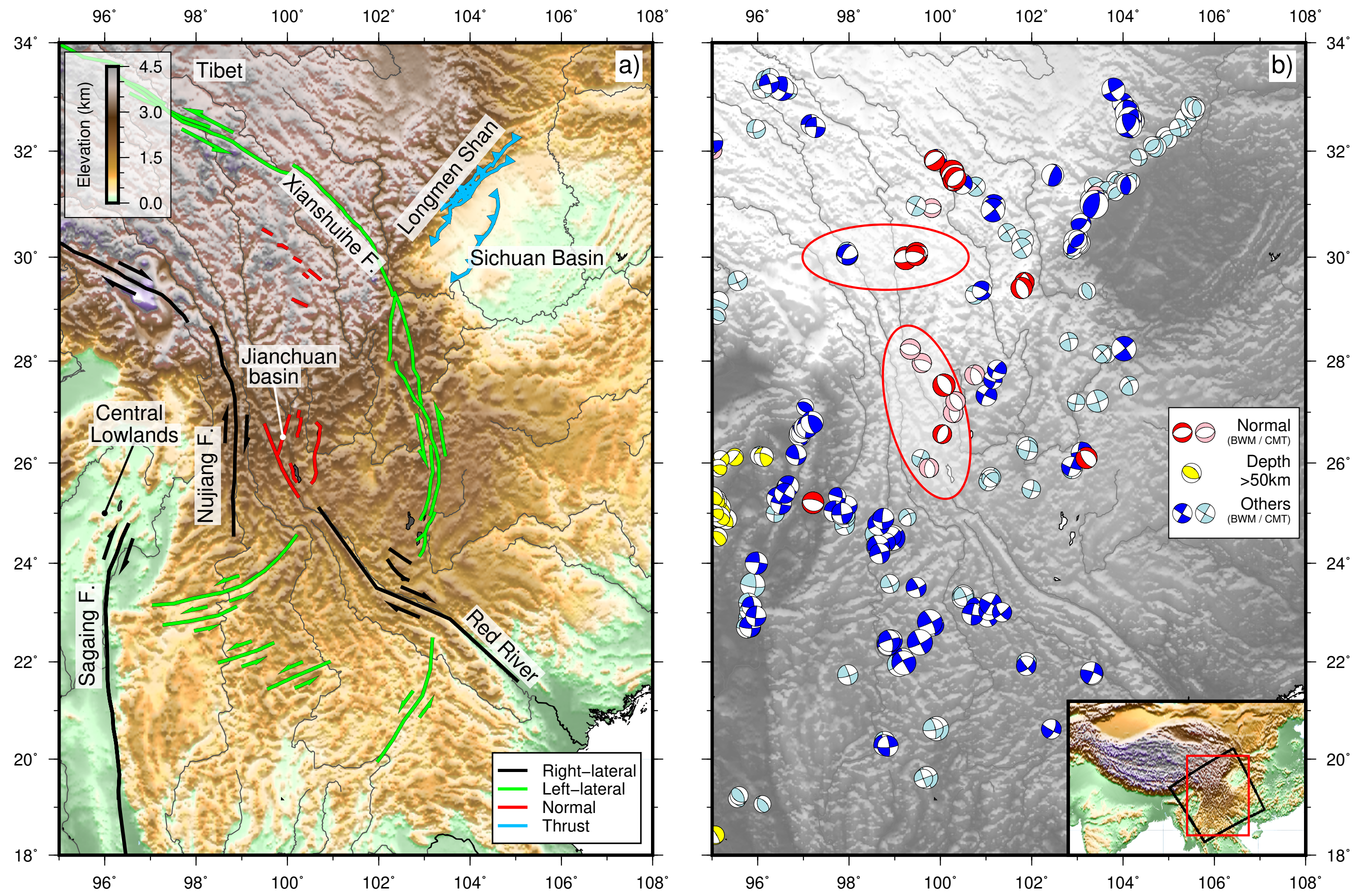

Figure 1: a) Major active faults in south-east Tibet, from Copley (2008); Hubbard and Shaw (2009). Black and green lines are right- and left-lateral strike-slip faults respectively. Note the opposite sense of shear adjacent to the Central Lowlands of Myanmar and Sichuan Basin. Red lines show normal faults. Blue lines show thrust faults with teeth on the hanging-wall side. b) Focal mechanisms of earthquakes in south-east Tibet. Focal mechanisms determined from body-waveform modelling from Copley (2008) (and references therein), Zhang et al. (2010), Li et al. (2011), Han et al. (2014), Bai et al. (2017), Han et al. (2018) are shown in red if they have a rake of -90±35° (normal faulting), and dark blue otherwise. Yellow focal mechanisms are >50 km deep and are associated with subduction beneath the Indo-Burman ranges, all other earthquakes have depths less than ∼20 km. Focal mechanisms in pink (normal faulting, with rakes of -90±35°) and pale blue are those from the CMT catalogue with >70% double couple and >10 depth phases in the EHB catalogue if the earthquake occurred before 2009. Two regions of normal faulting discussed in the text are circled in red. Red box in inset shows the figure's location, black box shows location of Figure 3.

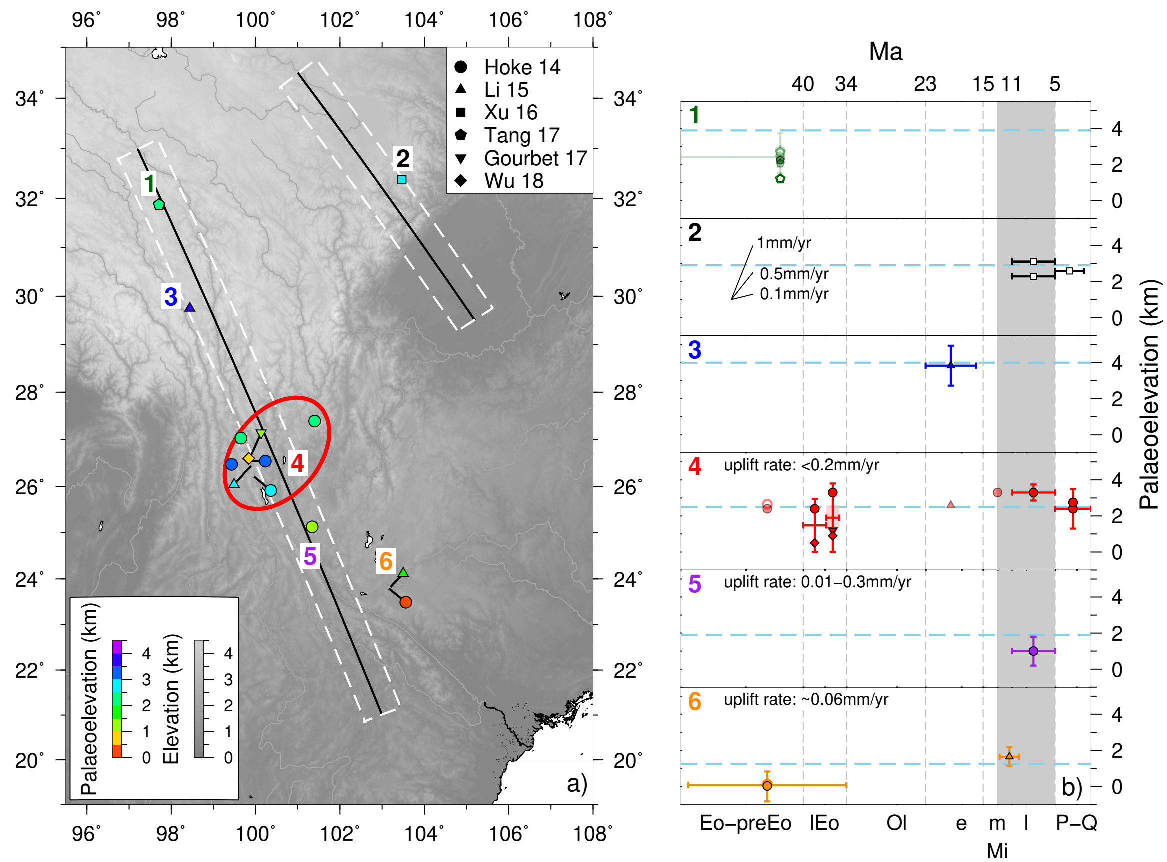

Figure 2: Results of stable-isotope palaeoaltimetry studies in south-east Tibet. a) Sample localities from Hoke et al. (2014); Li et al. (2015); Xu et al. (2016); Tang et al. (2017); Gourbet et al. (2017) and Wu et al. (2018) are coloured by palaeoelevation. 6 regions are labelled, which correspond to panels in b, the red ellipse indicates the extent of region 4. Black lines with white boxes show the regions plotted as topographic profiles in Figure 6g and h. b) Sample ages and palaeoelevations in each region. Epoch labels are – Eo-preEo: Eocene-pre Eocene >40 Ma, lEo: late Eocene: 40–34 Ma, Ol: Oligocene 34–23 Ma, eMi: early Miocene 23–15 Ma, mMi: middle Miocene 15–11 Ma, lMi: late Miocene 7–5 Ma, P-Q: Pliocene–Quaternary 5–0 Ma. Where multiple samples from the same author are reported in the same epoch in the same region only a single error bar (representing the highest and lowest palaeoelevation estimates) is plotted. Palaeoelevation estimates using a modern temperature-elevation relationship are shown as filled symbols, those using a higher Eocene temperature estimate are unfilled. The colour of symbols corresponds to their region in a). Pale-outlined points in regions 1 and 4 are the authors' original palaeoelevation/age inferences. Dark-outlined points show the revised palaeoelevations/ages from Gourbet et al. (2017) and Wu et al. (2018), which we use to determine uplift rates. In region 4 the pink rectangle corresponds to the range of palaeoelevation estimates derived from palynology by Wu et al. (2018). Symbol shapes are as in a). Grey bar shows the timing of increased exhumation and erosion rates suggested by Clark et al. (2005b) to indicate rapid uplift. Dashed blue lines indicate mean present-day sample-site elevation for each region.

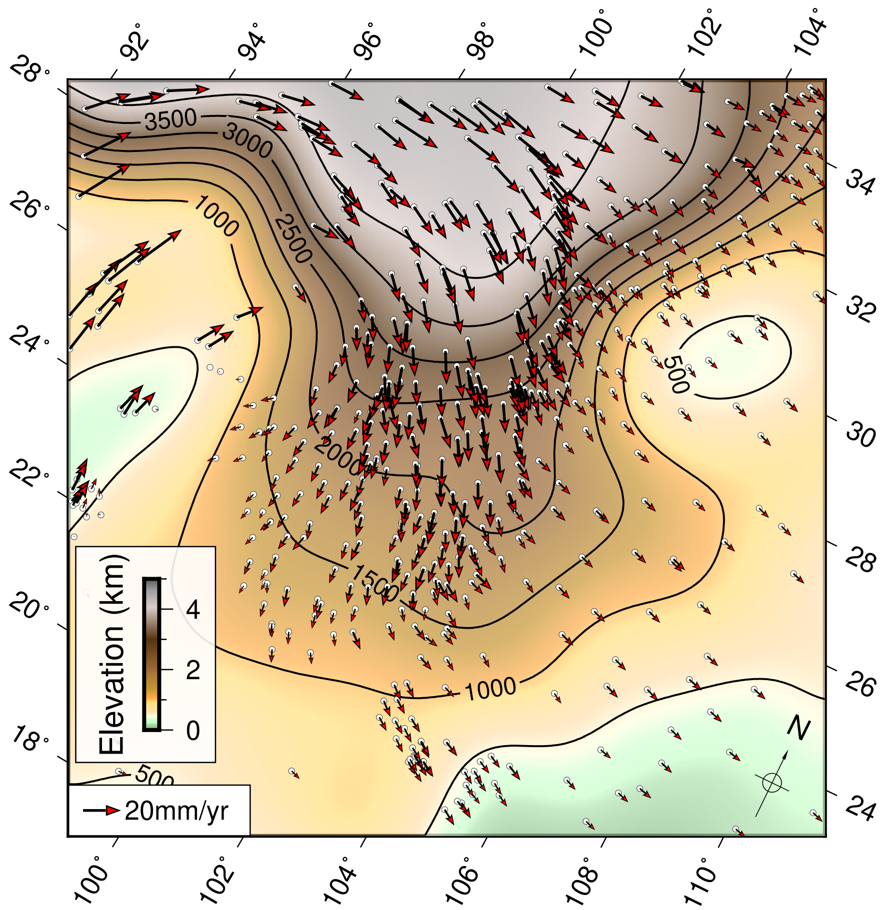

Figure 3: Topography of south-east Tibet after applying a low-pass 500 km-diameter Gaussian filter in an oblique Mercator projection (equator azimuth 60°, centred on 101.5° E, 26.5° N, location shown as black box in the inset of Figure 1b) for comparison to our model set-up (Figure 4) and results (Figures 5 and 8, Section 4). GPS velocities from Zheng et al. (2017) are shown in a Eurasia-fixed reference frame.

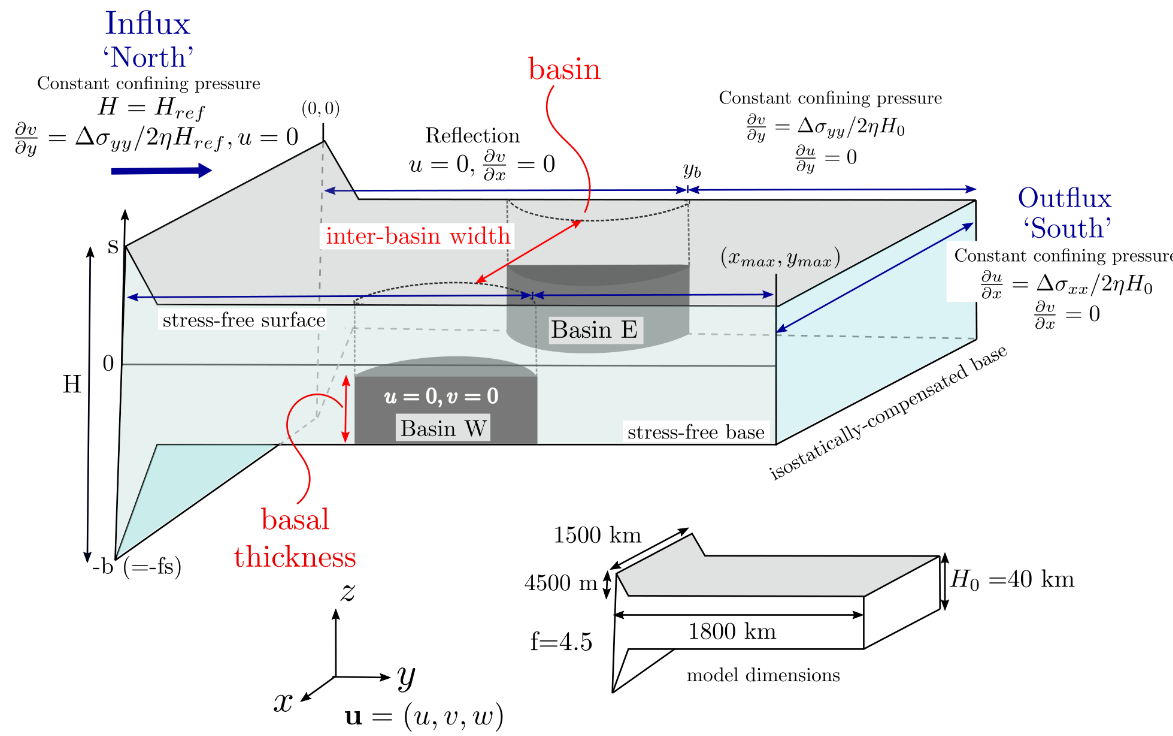

Figure 4: Model geometry, showing the initial topography and symmetric rigid regions. Boundary conditions on $x = x_{max}$ are the same as those on $x = 0$. Inset shows dimensions of model domain. The isostatic root is not shown to scale.

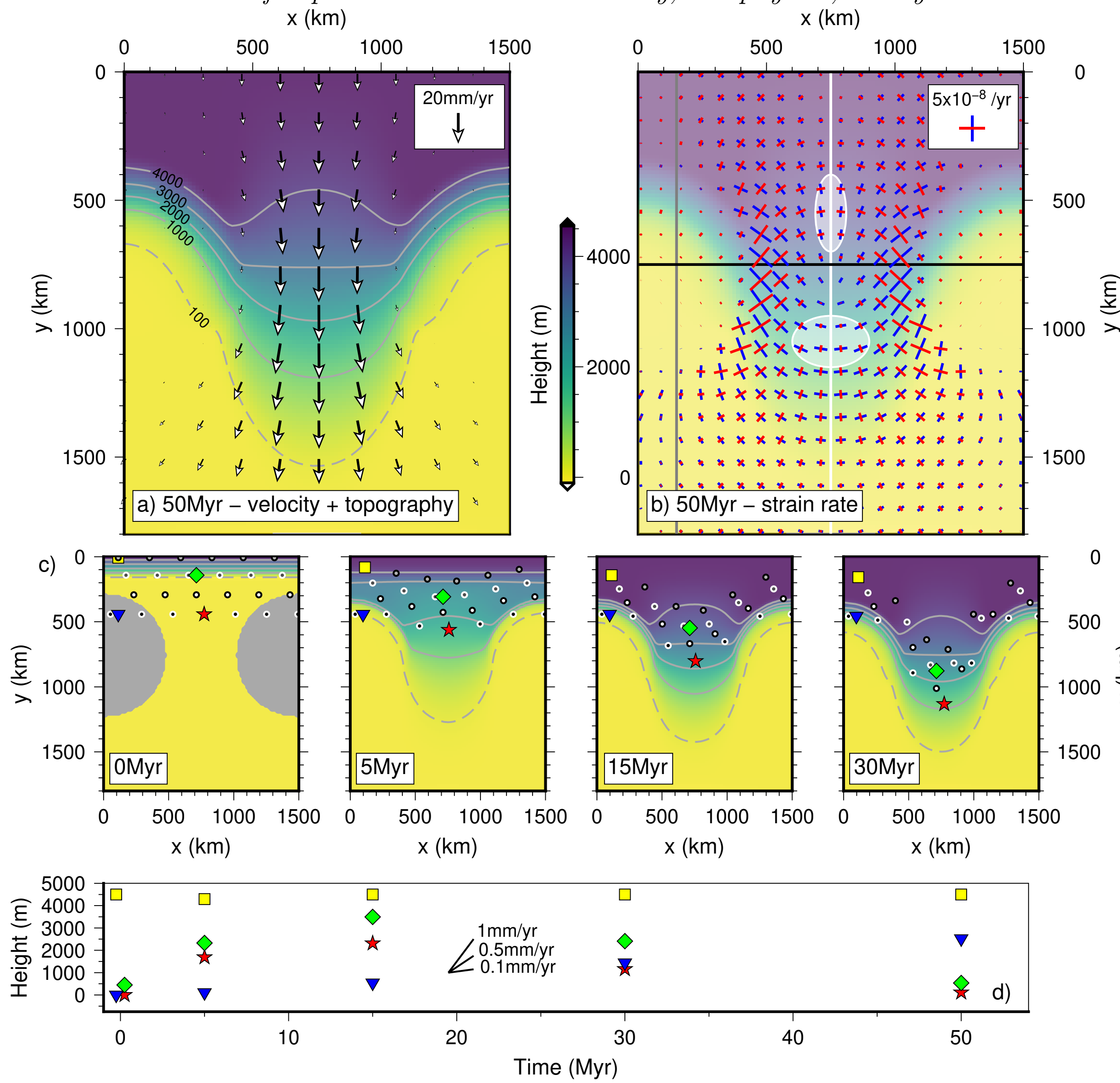

Figure 5: Modelling results for a symmetric model (both basins have the same size and location in y) with 450 km-radius basins (grey semicircles at 0 Myr in c) with a 15 km-thick rigid base. The influx boundary (left-hand side in Figure 4) is at the top of each panel. a) topography and velocities after 50 Myr for a fluid with a viscosity of 10^{22} Pas. Topography is plotted relative to the surface of 40 km-thick, isostatically-compensated crust and contoured at 100 m (dashed line), 1000 m, 2000 m, 3000 m and 4000 m. b) principal axes of the surface horizontal strain-rate tensor after 50 Myr. Blue bars are extensional, red bars are compressional. Gray, white and black lines show locations of profiles in Figures 6c, d and 7c respectively. White ellipses show the two regions where extensional strain rates are ∼2–5 times greater than compressional strain rates, discussed in Section 5. c) Evolution of topography through time. Dots show large-scale lateral transport of particles moving with the surface of the current and can be viewed as analogous to the motion of near-surface carbonates used for palaeoaltimetry (Section 3.2). Contours are at 100 m (dashed line), 1000 m, 2000 m, 3000 m and 4000 m. d) shows the elevation history of the shaped particles in c. Since the particles are advected with the current their elevation can decrease as well as increase.

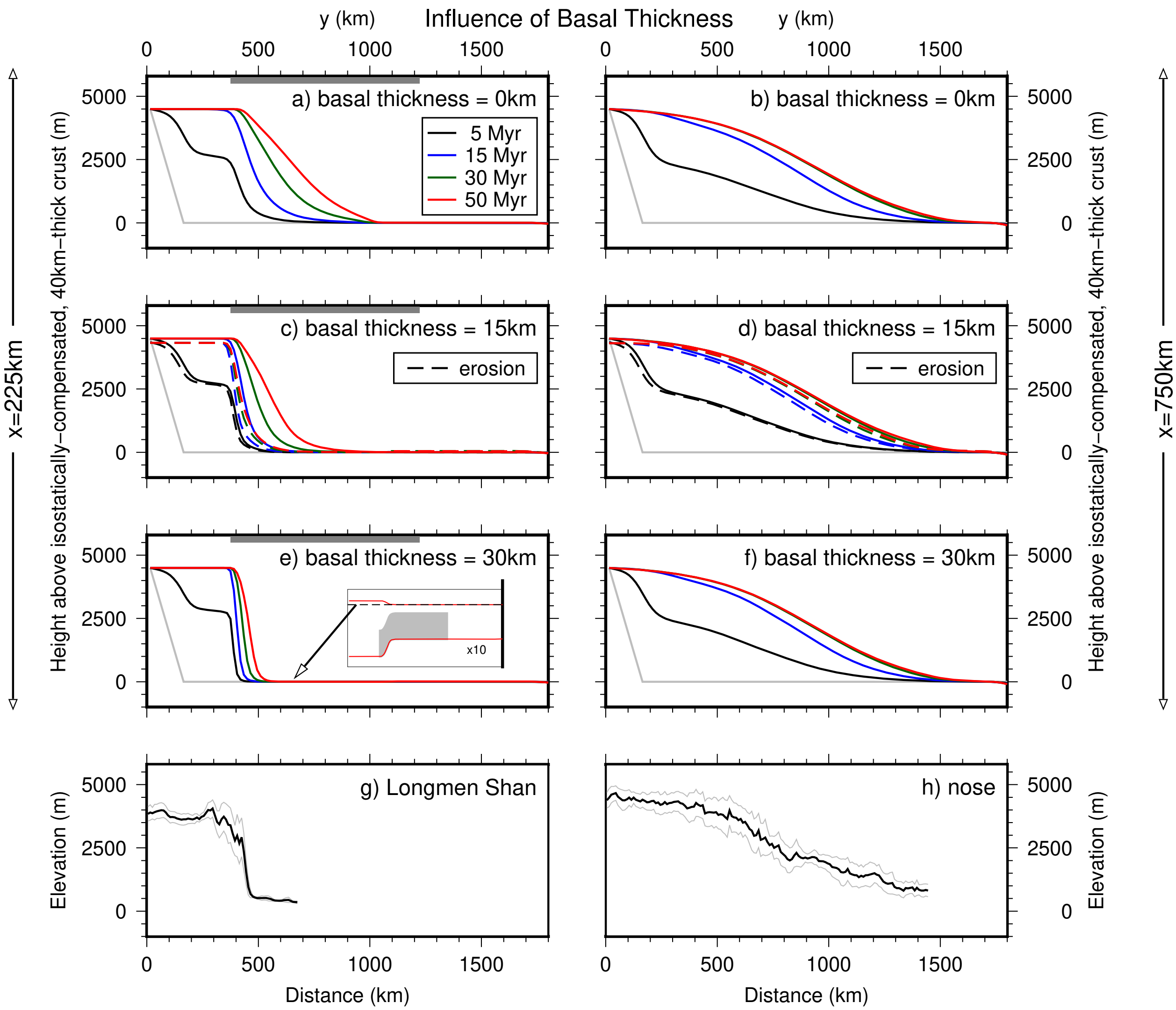

Figure 6: Effect of changing the basal thickness of the rigid basin (analogous to the thickness of undeforming lower crust) on the propagation of topography. The lateral extent of the basin which has a rigid basal thickness is indicated by the grey bars in a, c and e. a), c) and e) show profiles through the basin (gray line in Figure 5b) for basal thicknesses of 0 km (rigid base), 15 km and 30 km respectively . b), d) and f) show profiles through the inter-basin (stress-free base) region (white line in Figure 5b) for basal thicknesses of 0 km (rigid base), 15 km and 30 km respectively. The basal thickness has no significant effect on the development of topography in the regions with stress-free base. Elevations are relative to the surface of 40 km-thick, isostatically-compensated crust. Inset in e) shows the full thickness of the current (10x vertical exaggeration) to demonstrate how topography in this figure relates to full model. Grey region is the rigid basin. Dashed lines in c) and d) show the effect of erosion with $\kappa = 4$ mm yr^{-1} in equation (1). c and d are profiles through the same model shown in Figure 5. g) and h) show topographic profiles and standard deviation across the Longmen Shan and between the Sichuan Basin and Central Lowlands of Myanmar respectively (profile locations shown in Figure 2a), demonstrating the similarity of topographic gradients in south-east Tibet to those resulting from our model.

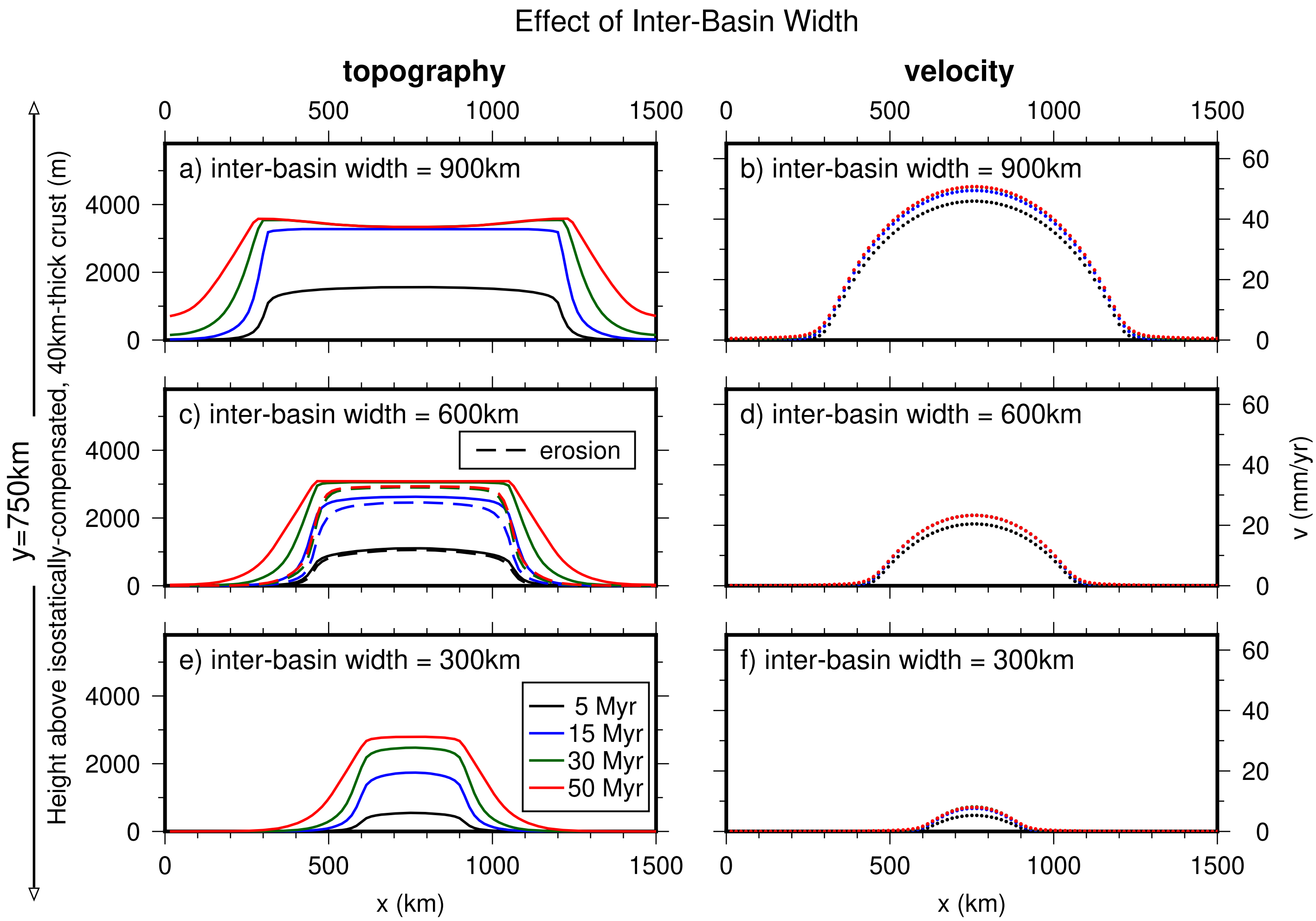

Figure 7: Effect of changing the distance between basins (inter-basin width, Figure 4). In each case profiles are taken at the centre of the semi-circular regions (black line in Figure 5b shows location of c and d), which have a basal thickness of 15 km. Elevations are relative to the surface of 40 km-thick, isostatically-compensated crust. a) and b) 900 km inter-basin width. a) shows the evolution of topography through time. The saddle arises because of thinning due to rapid velocities in the centre of the inter-basin region. b) the velocity perpendicular to the profile (v in Figure 4) after 50 Myr. c) and d) as for a and b but for an inter-basin width of 600 km. Note that c) and d) are profiles through the same model as Figure 5 and Figures 6c and d, with basin radius 450 km, inter-basin width 600 km and basal thickness 15 km. Dashed lines show the effects of erosion with $\kappa = 4$ mm yr^{-1} in equation (1). e) and f) as for a and b but for an inter-basin width of 300 km.

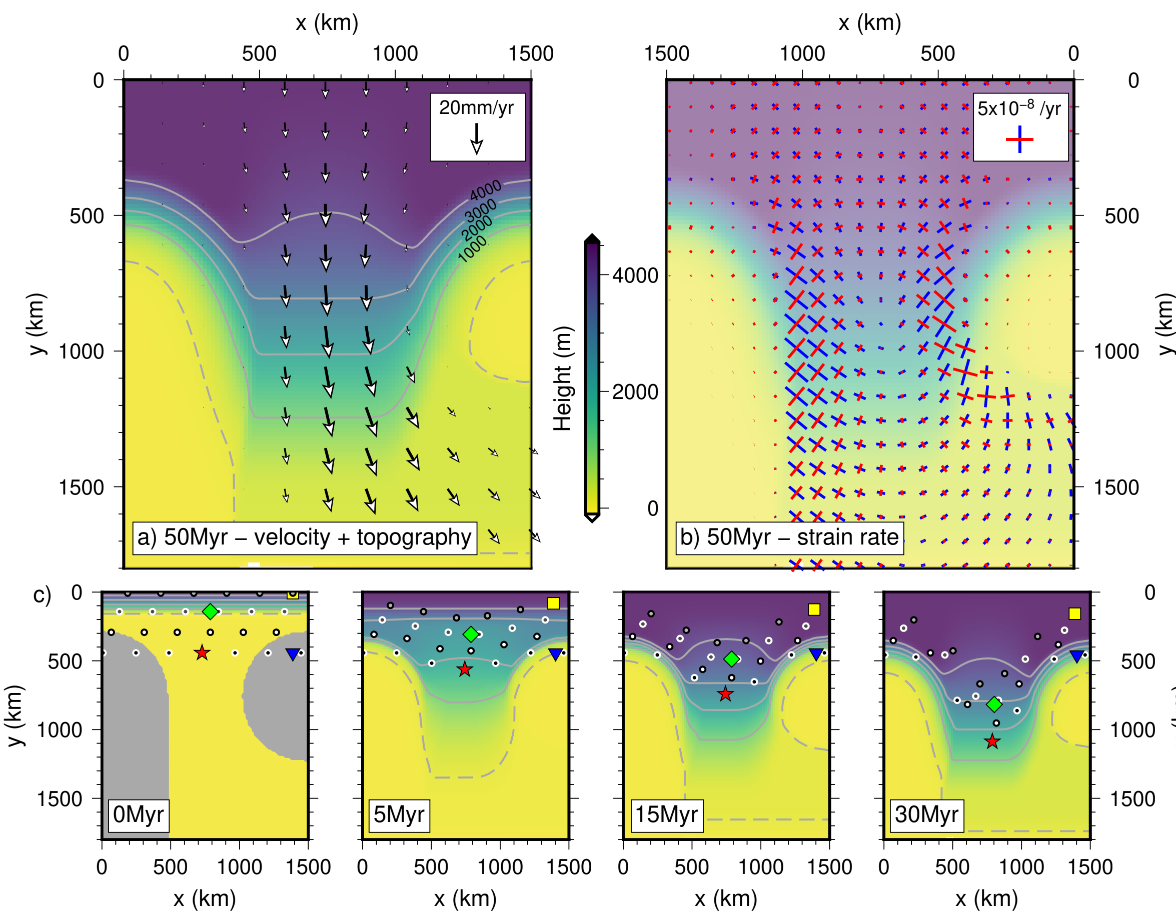

Figure 8: Modelling results for an asymmetric model set-up with 15 km basal thickness in the regions shown in grey in the 0 Myr panel of c. Panels are as for Figure 5. Note the broader region of shear adjacent to the extended basin.

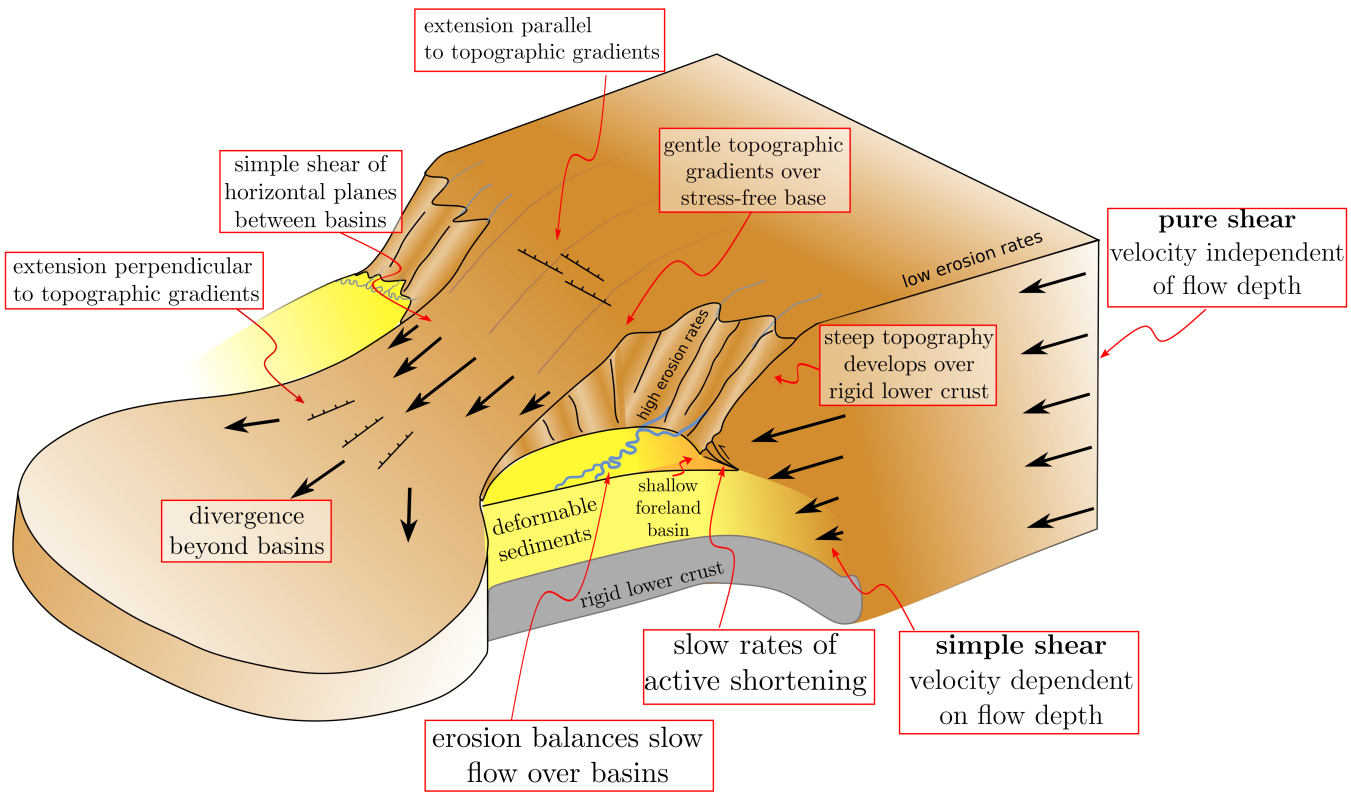

Figure 9: Cartoon showing effects of a rigid region on the development of topography. Steep topographic gradients develop above the region of rigid lower crust because of the dependence of velocity on flow depth. The compressional strain rates associated with growth of this steep topography are much less than the shear strain rates between basins. Regions with a stress-free base (without strong lower crust) deform by pure shear of vertical planes, which results in gentle topographic gradients. Between two rigid regions flow is dominated by simple shear of horizontal planes, similar to flow in a pipe. Beyond the basins the flow can spread out, leading to extension.

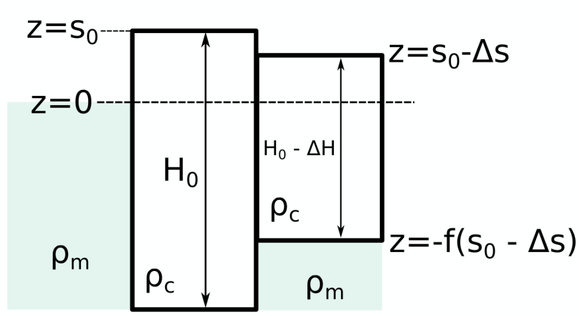

Figure A.1: Diagram to show isostatic balance used to find boundary conditions on $x = 0, x_{max}$. The column of mantle on the left hand side of the figure is to demonstrate that the reference level is set by a column of mantle. The deviatoric stress between the two columns of continental crust is calculated by integrating the pressure difference between them and dividing by the thickness (e.g. Artyushkov, 1973; Molnar and Tapponnier, 1978; Dalmayrac and Molnar, 1981; Turcotte and Schubert, 2014).